Aerodynamic Performance of an Adaptive Rear Wing at Different Angles of Attack

Boran Beyit Kolcu

Submitted to the
Institute of Graduate Studies and Research
in partial fulfillment of the requirements for the degree of

Master of Science
in
Mechanical Engineering

Eastern Mediterranean University
August 2022
Gazimağusa, North Cyprus

Approval of the Institute of Graduate Studies and Research

Prof. Dr. Ali Hakan Ulusoy
Director

I certify that this thesis satisfies all the requirements as a thesis for the degree of Master of Science in Mechanical Engineering.

Assoc. Prof. Dr. Murat Özdenefe
Chair, Department of Mechanical Engineering

We certify that we have read this thesis and that in our opinion it is fully adequate in scope and quality as a thesis for the degree of Master of Science in Mechanical Engineering.

Prof. Dr. Hasan Hacışevki
Supervisor

Examining Committee

1. Prof. Dr. Hasan Hacışevki

2. Assoc. Prof. Dr. Devrim Aydın

3. Asst. Prof. Dr. Ali Shefik

ABSTRACT

In this paper, computational fluid dynamics results are presented on an active rear wing designed based on the S1223 aerofoil profile. The rear wing was subjected to turbulent flow with the standard two equation k-ε turbulence model, using ANSYS Fluent software to study the aerodynamic behaviour and the force generating capabilities of the wing. The simulation was performed when the wing was set at four different angles of attack. Flow visualisation was performed to understand the nature of the air flow around the wing. Force components were additionally calculated for downforce and drag force comparison at different angles of attack, a maximum of 190.828 N and a minimum of 121.891 N of downforce was calculated. Drag force was 12.895 N at its minimum and a highest drag force of 19.518 N was calculated. It was found out that the S1223 aerofoil profile successfully aided the rear wing to generate downforce at relatively low angles of attack.

Keywords: automotive aerodynamics, downforce, computational fluid dynamics.

ÖZ

Bu çalışmada, S1223 hava folyosu profiline sahip bir aktif arka kanat'ın hesaplamalı akışkanlar dinamiği sonuçlarına yer verilmiştir. Arka kanat k-ε türbülans modeli kullanılarak türbülanslı akışa tabi tutulmuştur. Arka kanat dört farklı hücum açısı kullanılarak simülasyona tabi tutulmuştur, Arka kanat etrafından akan havanın doğasını anlayabilmek için akış görselleştirme kullanılmıştır. Ayrıca, farklı hücum açılarındaki yere basma kuvveti ve sürüklenme kuvvetlerini karşılastırmak için farklı kuvvet öğeleri hesaplanmıştır, maksimum 190.828 N ve minimum 121.891 N bastırma kuvveti hesaplandı. Sürükleme kuvveti minimumda 12.895 N ve maximumda 19.518 N olarak hesaplandı Çalışmanın sonucunda, S1223 hava folyosu profilinin arka kanat'ın düşük hücum açılarında yere basma kuvveti üretiminde faydalı olduğu ortaya çıkmıştır.

Anahtar Kelimeler: otomotiv aerodinamiği, yere basma kuvveti, hesaplamalı akışkanlar dinamiği.

ACKNOWLEDGMENT

I should mention that I am highly grateful that Prof. Dr. Hasan Hacişevki has supervised me for two years all through this project and never withhold his advice and assistance. Beyond all, he has been highly enthusiastic about my work and encouraged me all through the project. His ideas and experiences shone a guiding light to this project, which will forever be appreciated.

I would also like to pay my gratitude to Ms. Zahra Pezeshki who helped me intensively through the simulation process of this study. She has always been patient to my all my questions and never withhold her help as far as her knowledge and experience allowed her to do.

TABLE OF CONTENTS

ABSTRACT iii

ÖZ iv

ACKNOWLEDGEMENT v

LIST OF TABLES viii

LIST OF FIGURES ix

LIST OF SYMBOLS AND ABREVIATIONS xi

1 INTRODUCTION 1

1.1 Aerodynamics in Road Vehicles 1

1.2 Angle of Attack 3

1.3 Yaw Angle 3

1.4 Handling Stability 4

2 LITERATURE REVIEW 5

2.1 Free-stream Aerodynamics 5

2.2 Aerofoils 12

3 METHODOLOGY 15

3.1 Designing the Rear Wing 15

3.2 CFD Simulation 17

3.2.1 Simulating the Wind Tunnel Environment 18

3.2.2 Mesh Structure 19

3.2.3 Boundary Conditions 23

4 RESULTS AND DISCUSSION 27

4.1 Residuals 27

4.2 Flow Visualisation 29

4.2.1 Flow Visualisation on the Wing at 0° Angle of Attack 30
4.2.2 Flow Visualisation on the Wing at 2° Angle of Attack 33
4.2.3 Flow Visualisation on the Wing at 4° Angle of Attack 36
4.3 Downforce and Drag Force 39
4.4 Negative Angle of Attack 40
4.5 Discussion 42
4.5.1 Aerodynamic Performance of the Rear Wing 43
4.5.2 Velocity and Pressure Contours 47
4.5.3 Velocity Vectors and Streamlines 50
4.5.4 Aerodynamic Behaviour of the Wing at Negative Angle of Attack 54
5 CONCLUSION 56
REFERENCES 59

LIST OF TABLES

Table 1: Dimensions of the fluid enclosure around the wing. 19

Table 2: Mesh information. 20

Table 3: Flow and turbulence boundary conditions. 24

Table 4: All three velocity components and turbulence variables. 26

Table 5: Standard k-ε turbulence model constants. 26

Table 6: Downforce and drag force data calculated at three different angles of attack. 39

Table 7: Downforce and drag force data calculated at negative 4° angle of attack. .. 42

Table 8: Downforce coefficients compared to scientific literature [7]. 43

Table 9: Drag force coefficients compared to scientific literature [7]. 43

LIST OF FIGURES

Figure 1: 1: 25 scale Honda CR-X del Sol model from the study of Kurec et al [7]... 5

Figure 2: Wind tunnel setup [7]. 7

Figure 3: Flow visualization data with spoiler at 0° and 55° respectively [7]. 8

Figure 4: Oil flow visualizations on the suction surface of the wing [7]. 11

Figure 5: S1223 aerofoil profile: specialised for high lift and low Reynolds numbers. 16

Figure 6: (a), (b); Rear wing design with S1223 aerofoil profile..... 16

Figure 7: Rear wing in a fluid enclosure. 19

Figure 8: Mesh structure on the fluid domain and the rear wing. 20

Figure 9: Mesh structure on the fluid domain and the rear wing from a higher point of view. 21

Figure 10: Finer mesh on the leading edge of the rear wing. 21

Figure 11: A closer look at the finer mesh on the leading edge of the rear wing. 22

Figure 12: Finer mesh on the trailing edge of the rear wing. 22

Figure 13: A closer look at the finer mesh on the trailing edge of the rear wing. 23

Figure 14: Inlet and outlet air flow illustration. 25

Figure 15: Residuals of the simulation of rear wing with 0° angle of attack. 27

Figure 16: Residuals of the simulation of rear wing with 2° angle of attack. 28

Figure 17: Residuals of the simulation of rear wing with 4° angle of attack. 28

Figure 18: The plane where the flow was visualised on. 29

Figure 19:Velocity contour of the wing at 0° angle of attack. 30

Figure 20: Stagnation point on the leading edge of the wing at 0° angle of attack. .. 31

Figure 21: Pressure contour of the wing at 0° angle of attack. 31

Figure 22: Velocity vectors of the wing at 0° angle of attack. 32
Figure 23: Streamlines on the middle plane of the wing at 0° angle of attack. 32
Figure 24: Streamlines at the trailing edge of the wing at 0° angle of attack. 33
Figure 25: Velocity contour of the wing at 2° angle of attack. 33
Figure 26: Stagnation point on the leading edge of the wing at 2° angle of attack. .. 34
Figure 27: Pressure contour of the wing at 2° angle of attack. 34
Figure 28: Velocity vectors of the wing at 2° angle of attack. 35
Figure 29: Streamlines on the middle plane of the wing at 2° angle of attack. 35
Figure 30: Streamlines at the trailing edge of the wing at 2° angle of attack. 36
Figure 31: Velocity contour of the wing at 4° angle of attack. 36
Figure 32: Stagnation point on the leading edge of the wing at 4° angle of attack. .. 37
Figure 33: Pressure contour of the wing at 4° angle of attack. 37
Figure 34: Velocity vectors of the wing at 4° angle of attack. 38
Figure 35: Streamlines on the middle plane of the wing at 4° angle of attack. 38
Figure 36: Streamlines at the trailing edge of the wing at 4° angle of attack. 39
Figure 37: Velocity vector of the wing at negative 4° angle of attack. 40
Figure 38: Pressure contour of the wing at negative 4° angle of attack. 41
Figure 39: Streamlines on the middle plane of the wing at negative 4° angle of attack. 41
Figure 40: Streamlines at the trailing edge of the wing at negative 4° angle of attack. 42

LIST OF SYMBOLS AND ABREVIATIONS

α	Angle of Attack (°)
ε	Turbulence Dissipation Rate (m^2/s^3)
μ	Dynamic Viscosity (m^2/s)
μ_t	Turbulent Viscosity (m^2/s)
ω	Specific Turbulence Dissipation Rate (m^2/s^3
A	Frontal Area (m^2)
ABS	Antilock Braking System
AKN	Abe-Kondoh-Nagano Low Reynolds Number K-epsilon Model
ANSYS	Analysis of Systems
Atm	Atmospheric Pressure
BMW	Bayerishe Motoren Werke (Bavarian Engine Works)
CAD	Computer Aided Design
C_D	Drag Coefficient
CFD	Computational Fluid Dynamics
C_L	Lift Coefficient
CR-X	Civic Renaissance Experimental
D	Downforce (N)
EV	Electric Vehicle
F_D	Drag Force (N)
FW-H	Ffowcs Williams-Hawkins Model
h	Ground Clearance (m)
ICE	Internal Combustion Engine
k	Turbulence Kinetic Energy (m^2/s^2)

L	Vehicle Length (m)
LDA	Laser Doppler Anemometry
LES	Large Eddy Simulation
NACA	National Advisory Committee for Aeronautics
NASCAR	National Association for Stock Car Racing
RANS	Reynolds-averaged Navier-Stokes equations
Re	Reynolds Number
RKE	Realizable K-epsilon Model
RNG	Reynolds Normalization Group
SAE	Society of Automotive Engineers
SAS	Scale Adaptive Simulation
SST	Shear Stress Transport
Ti_2O	Titanium(II) Oxide

Chapter 1

INTRODUCTION

1.1 Aerodynamics in Road Vehicles

It is convenient to specify the term “high-performance vehicles” as road vehicles which basically possess high power-to-weight ratio. Rapid acceleration, deceleration, and precise cornering and manoeuvrability are crucial factors that determine the overall performance of a race car / sports car. Race cars are subjected to a process called homologation which forces cars to compete with similar vehicles, under certain rules which decide the maximum performance of vehicles [1].

In order to obtain good performance out of a car, strong attention should be paid to its aerodynamic properties as reduced drag and enhanced downforce are a couple of basic factors that benefit to the acceleration, top speed, and cornering of cars. For any given EV (electric vehicle) or ICE (internal combustion engine) powered car, reduced drag determines the top speed and acceleration values. Drag can be altered by two factors; drag coefficient ‘C_D’ and frontal area ‘A’ (which is the area of the front view of the vehicle). When it comes to handling, chassis structure, suspension set up, tyre size and compound are the main governing factors of cornering characteristics. However, at high speeds, aerodynamics is of great importance when vehicle stability is concerned [2].

Downforce on high-performance cars can be generated by two flow regimes; free-stream (flow around a rear wing) and ground effect (flow around a front wing and/or a diffuser) aerodynamic. Downforce generation is the primary area of concern of ground effect aerodynamics when it comes to race cars and it is generated by creating a low-pressure zone near the parts of the race car which are close to the ground or even in between the undertray and the ground, as well as utilizing inverted wings to generate negative lift in free-stream flow conditions.

The parts of a race car which supply downforce by ground effects is aerodynamically more efficient when compared to the parts that operate in free-stream conditions. Downforce enhancement on race cars plays an important role on reducing the lap times. The racing industry is on the top of the ladder when comes to technology innovation, and is an eligible training ground for engineers as well as engineering students with Formula Student programmes in European universities. In many countries like Britain and Italy, racing industry covers a major area in technology engineering industry. There is a continuous demand, and even necessity, for the improvement of performance in the racing world, hence, aerodynamics is a crucial area where car companies can invest in, investigate and improve upon on its own [3][4][5].

Racing industry is not, of course, the only area of automotive engineering that can benefit from a clever and outstanding aerodynamics design. The cooperation of designers and aerodynamicists play a superior role in the performance of both race cars and road legal passenger cars. No matter whether the area of interest is family saloons or hyper cars, close attention is paid to the aerodynamic parts of the cars; for example,

wings, diffusers, air intakes, and Gurney flaps together with various other design parameters and regulations.

1.2 Angle of Attack

The assumption of constant aerodynamic drag is not an accurate and valid assumption in real-life scenarios. For example, when driving over a hill or a bump on the road surface the suspension of the vehicle stretches and compresses, adjusting the dampening and stiffness due the vertical movement of the vehicle body. This results in altered angle of attack of aerofoils present on the vehicle, changing the flow around the car altering aerodynamic properties. Several studies revealed that widely used front suspension settings amplify these movements; downforce tends to decrease during the rebound (coming back to usual suspension position) [2].

1.3 Yaw Angle

Both side wind and cornering may result in yawed air flow. Various tyre compounds have different slip angles which basically help the vehicle's cornering characteristics, that slip angle can be the same as the yaw angle. Usually, the slip angles are 10° and 8° for road and race tyres respectively.

The yaw angle due to side winds and cornering may cause the drag force to increase and the downforce to decrease. In order to maintain vehicle stability under these consequences, the lift forces at the rear end should be considerably higher than that at the front end. However, excessive downforce at the rear can cause the vehicle to understeer during cornering. Similarly, excessive downforce at the front axle results in oversteer. The forces acting on the vehicle should be balanced as far as possible for better performance.

The pressure centre of the vehicle is of major importance under yawed airflow conditions. The yawing moment has the tendency to force the vehicle to “turn away” from the air flow direction if the pressure centre is located far ahead of the centre of gravity. The opposite effect arises if the pressure centre is positioned far behind the centre of gravity, the car “turns into” the air flow direction due to yawing moment. This is more desirable as it increases cornering stability.

Since the aerodynamic forces and side forces due to wind act towards the inside of the corner, they result in a stabilizing effect if the centre of gravity and centre of pressure is positioned correctly with clever design. On the other hand, this relationship can be altered if the downforce acting on the vehicle is lost [2].

1.4 Handling Stability

Assmann et al. were interested on the effects of different aerodynamic coefficients on simulated driving manoeuvres; steady-state cornering, cutting the power off during a corner, steering step input, and cross-wind. It was found out that the understeer can be minimised by lowering the lift coefficient at the front end. The stability was improved by increasing the lift coefficient at the rear end, which resulted in better manoeuvrability. The acceleration of the vehicle was seen to be improved by reduced overall lift. In addition to this, handling was seen to be improved by decreasing the lateral force coefficient on the vehicle. It was seen that high value of yawing moment had the tendency to the destabilise the car. The rolling moment had almost no considerable effects during the simulations [6].

Chapter 2

LITERATURE REVIEW

2.1 Free-stream Aerodynamics

Kurec et al. investigated the flow over a 1:25 scale Honda CR-X del Sol model, mounted with both a rear wing and rear spoiler. The experimental data obtained by wind tunnel tests was compared with numerical data simulations based on four different turbulence models. The wing and the spoiler were controlled by several servo mechanisms and simulated the motion of active aerodynamic elements. The wing was tested under conditions of angle of attack ranging from 0° to 50°, increasing by increments of 5°. The spoiler was set at either at a horizontal setting of 0° or 55° [7].

Figure 1: 1:25 scale Honda CR-X del Sol model from the study of Kurec et al [7].

The wing used by Kurec et al. has so called “swan neck” mountings, which are becoming highly popular in the racing industry and high-end sports cars. The main

advantage of that kind of rear wing is the mountings do not affect the flow over the lower surface (suction side) of the wing simply because the mountings are connected the upper surface (pressure side) of the wing. That way, the flow over the suction side is not altered by the mountings. The aerofoil profile used for the investigation was called Tx1645 which has a similar profile to the Be153-175 aerofoil. The wing consists of two identical aerofoils connected together by a centre plate. Each aerofoil had 0.317 m wing span and 0.130 m cord length. Similarly, two identical spoilers were created and controlled as one single unit by two servomechanisms. The dimensions of the spoilers were by the trunk of the car model, this resulted in each spoiler element having a width of 0.226 m on height of 0.032 m. Spoilers could not be extended all the way up to the side plates of the wing due to the rounded shape of the trunk [7].

Experimental tests were performed in a closed loop wind tunnel which is 2.5 m wide and 2 m high, where the average flow velocity was set to be 23 m/s. The average turbulent intensity was set to be 3.5 % and turbulent length was 5 mm. Data based on drag force and downforce coefficients was collected. The downforce coefficient was seen to reach a local maximum around 25°. The most obvious difference was observed to be when the spoiler was positioned at 55°, it maximized the downforce and prevented stall, by directing the air flow over the trunk to the rear wing[7].

Figure 2: Wind tunnel setup [7].

The benefits obtained by utilizing a spoiler was discussed as such that the downforce, when the wing was moved from 5° angle of attack to 20°, observed to be 50% higher when the spoiler was positioned at 55°, in comparison with spoiler at horizontal position. The downforce coefficient was seen to be risen from 0.6 to 0.9. Kurec et al. stated that this provided the benefit of easy operation of small aerodynamic elements, such as the spoiler in that case since it requires less energy to move and is able to respond quicker to changes in the flow [7].

The findings of Kurec et al. further investigated by flow visualization on the rear wing. The wing was set at various angles of attack ranging from 1° to 25° and the spoiler at both 0° and 55°. An oil flow visualization with a mixture of silicon oil and Ti_2O was performed on one of the wing aerofoils (left to the centre plate). On the other aerofoil element (right to the centre plate), a much more traditional tuft flow visualization was performed by using five rows of 2.5 cm long strings attached to the suction side of the wing. A camera was positioned such that it captured the suction surface of the wing together with the spoiler and the mountings [7].

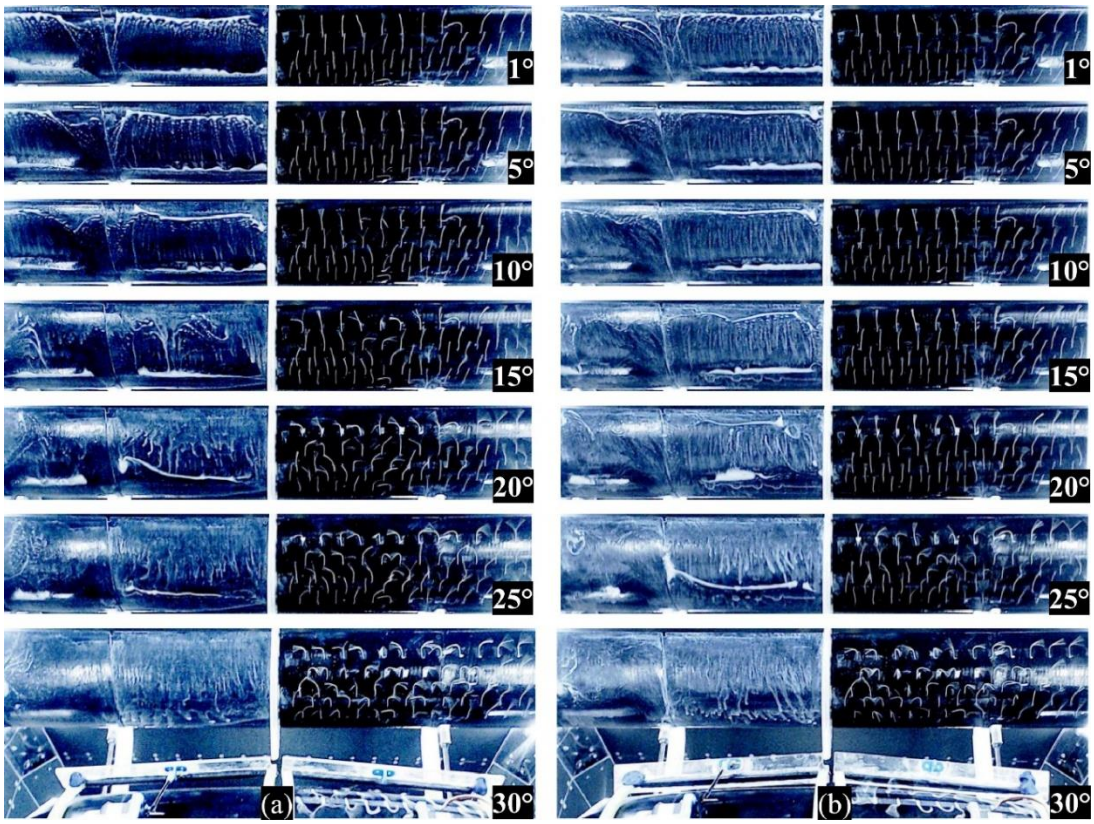

Figure 3: Flow visualization data with spoiler at 0° and 55° respectively [7].

Oil flow visualization revealed a flow pattern similar to that of low Reynolds number flow, where transition from laminar flow to turbulent took place. The Reynolds number for the whole car model for the experiment of Kurec et al. was equal to 2.51e+6, whereas the Reynolds number for the rear wing as a single unit was 1.89e+0.5 which is in the region of laminar-turbulent transition. A laminar oil bubble on the suction surface of the wing was captured by the camera, however, this laminar bubble encountered with the wake resulted by the mounting arm of the wing. A fully developed turbulent flow took place after the transition. Kurec et al. stated that the laminar bubble was short enough to not have an effect on the performance of the wing which would otherwise alter pressure distribution [7].

When Genç et al. investigated the low Reynolds number flow over a NACA2415 aerofoil at an agnle of attack of 15°, similar flow pattern was observed with a laminar

-turbulent transition process. The Reynolds number was found out to be equal to 2e+5. However, Genç et al. investigated solely on the aerofoil itself and supplied more insight to the aerodynamic performance of the NACA2415 aerofoil [8].

Flow visualisation performed by Kurec et al. also proved that the position of the spoiler enhanced the downforce generated by the wing. When the spoiler is positioned horizontally, the flow is mostly separated over the suction side of the aerofoil when the wing reached an attack angle of 15° and it is almost totally separated after 30° of angle attack. On the other hand, when the spoiler was at 55°, the flow was observed to be attached to the suction side of the wing even at angles of attack equal to 15° and 20°. The flow started to separate at 25° and was completely separated at 30 [7].

In order to obtain further validation Kurec et al. performed numerical analysis on ANSYS Fluent using five different Reynolds-averaged Navier Stokes (RANS) turbulence models.

The Realizable k-ε and Shear Stress Transport k-ω models are in fact the most widely used turbulence models when performing flow simulations [9]. Transition k-kl- ω and Transition SST are generally chosen to be used when there is laminar-turbulent transition is suspected. Engineers often choose to use SAS SST model to also investigate transition processes with additional intermittency equations [7].

When the turbulence models mentioned above were used by Kurec et al. it showed that, neither of the models resembled the experimental downforce and drag coefficients measurements thoroughly over the complete range of angles of attack and spoiler positions. However, it was found out that the SST k-ω and the Transition SST models

provided results closer to the experimental data for the spoiler at horizontal position. The RKE and the Transition k-kl-ω models resulted in similar results to the experiments for attack angles over 15°. When the results were observed, SAS SST seemed to be the most accurate turbulence model [7].

Results obtained from oil flow visualizations were also validated by the numerical analysis. Kurec et al. performed streamline visualisation by wall shear on the suction surface of the rear wing, as well as providing velocity contours over the wing. All five turbulence models displayed the flow attachment and separation phases when the attack angle was equal to 1° and 20° with the spoiler at 0° and 55°. Streamline visualization showed close resemblance with the oil flow visualization with the wing at 1° and spoiler at 55°. The Scale Adaptive Simulation SST and the Transition SST models showed a similar separation zone to that obtained by experimental approach [7].

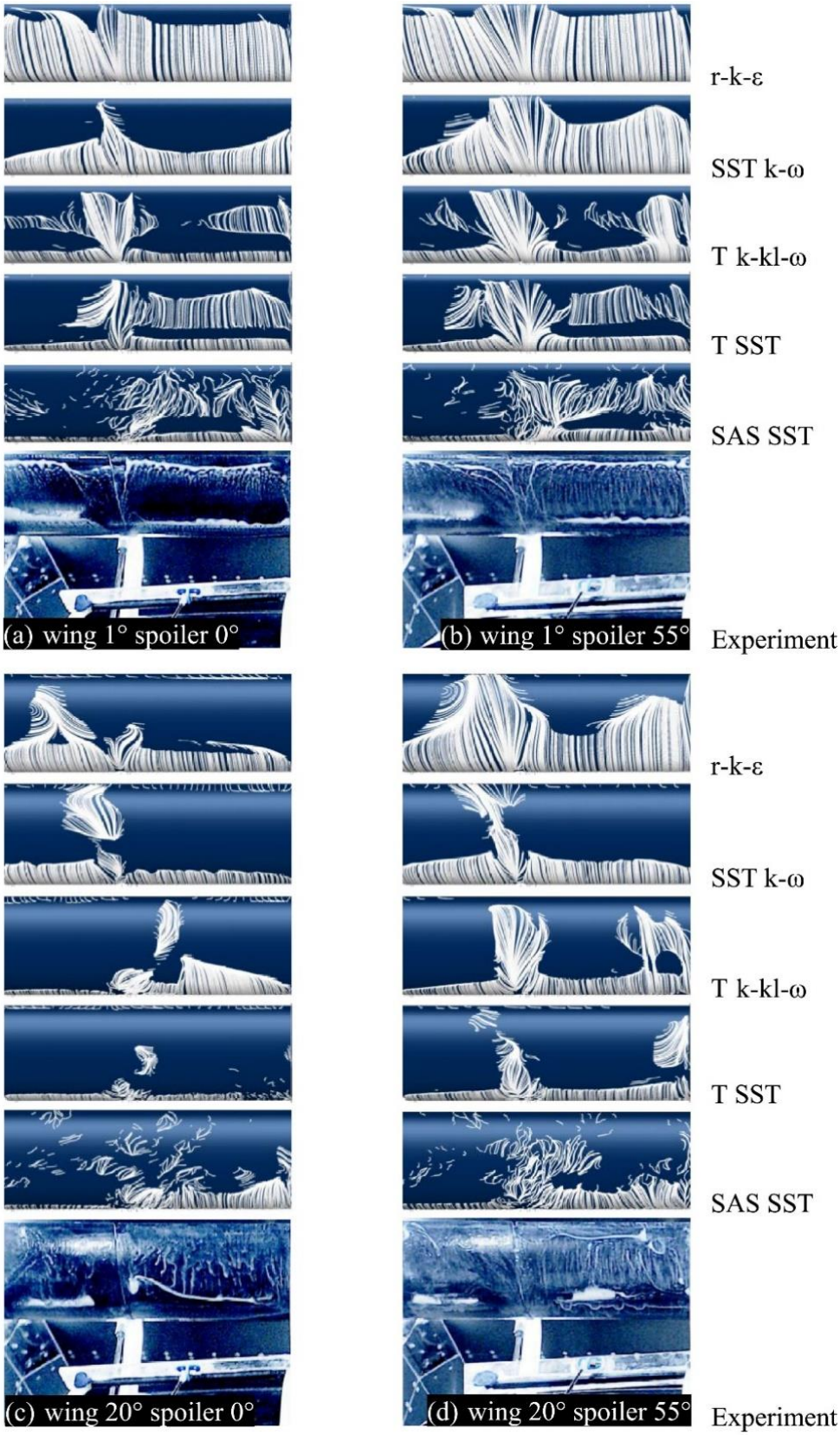

Figure 4: Oil flow visualizations on the suction surface of the wing [7].

When the wing is at 20 and the spoiler is at 55, experimental data showed that the flow was partially attached to the suction surface of the wing. This case was proven to be the same for SAS SST, Transition k-kl- ω and the RKE. On the other hand, the remaining two turbulence models showed the flow to be thoroughly separated [7].

2.2 Aerofoils

Aerofoils play a major role when it comes to designing front or rear wings, and diffusers. Low Reynolds number (Re) aerodynamics have become increasingly popular over the years with the recent aerodynamic developments in automotive, renewable energy, and airspace industries.

Low Reynolds number air flows has got the potential to cause harm on the air flowing over an aerofoil; laminar separation bubble potentially leads to a reduction in lift/downforce while also increasing the drag force acting on the body. All of these combined leads to unstable behaviour due to catastrophic air flow [10]–[12].

Many investigators performed experiments in order to understand the nature of the laminar separation bubble. How-wire anemometer and an oscilloscope were used by Gaster in an experiment on the laminar separation bubble. That particular study was performed over a wide range of Reynolds numbers and pressure distributions, and revealed that the way which the laminar bubble bursts is closely related with Reynolds number and pressure rise.

In another study, Tani classified the laminar bubble into two separate forms; these being called long and short bubble. The major finding of that study was the fact that when Re number was decreased the short laminar bubble burst at high angles of attack. This in turn resulted in the formation of a long bubble and flow separation. Rinioie and

Takemura investigated a NACA0012 aerofoil and at which angles of attack the laminar bubble forms. They have found that at angle of attack lower than 11.5° short bubble formed, and at angles of attack higher than 11.5° long bubble formed [13]–[15].

Oil flow visualisation has been proven to be a sufficient experimental tool in visualising air flow by various studies as mentioned elsewhere in this report. Sharma and Poddar also utilised this technique to visualise the air flowing over a NACA0015 aerofoil.

The objective of that study was to investigate the laminar separation bubble and transition process from laminar to turbulent flow. Sharma and Poddar investigated the aerofoil at various angles of attack at low Re number flows. It was concluded that the laminar bubble moved towards the leading edge of the aerofoil as the angle of attack was increased and then burst at a particular angle of attack, stalling the aerofoil. It was possible that the aerofoil entered the downforce reduction zone [16].

Genç et al. studied the laminar separation bubble phenomenon on a NACA2415 aerofoil experimentally, at low Re numbers. Their study clearly showed the formation process of the bubble, separation, transition, and re-attachment. It was stated that the transition flow laminar to turbulent took place at the point of highest pressure on the suction surface of the aerofoil.

Another major finding was the fact that the angle of attack at the which aerofoil stalled decreased together with the intensity of stall as the Re number was increased. Genç et al. also utilised the oil flow visualisation technique in order to clearly observe the transition process. It was found out that the separation point; laminar separation

bubble, moved towards the leading edge of the aerofoil as the angle of attack was increased at all Re numbers; which states that Genç et al. reached the same conclusion and Sharma and Poddar which was stated previously. Oil flow visualisation guided Genç et al. through observing the formation and progress of the laminar separation bubble and flow re-attachment. Genç et al. concluded that at low Re number flows, short laminar bubble burst at higher angles of attack leading to the formation of long bubble; which was also concluded by Tani [8], [14], [16].

Based on the knowledge obtained from the literature reviewed above, it was decided to perform CFD investigation on a rear wing based on the S1223 aerofoil profile in turbulent conditions at four different angles of attack, using the ANSYS Fluent software.

Chapter 3

METHODOLOGY

3.1 Designing the Rear Wing

For the purposes of this study, the CFD simulation was performed on rear wing design based on the S1223 aerofoil profile which can be seen in Figure 12. The S1223 aerofoil is known be specialised in generating high lift forces and relatively low Reynolds numbers, however sine the aerofoil profile is obviously used generate lift it was convenient to simply turn the profile upside down and use for negative lift (downforce) generation. Once the rear wing has been designed, which can be seen in Figure 13 (a) and (b), it went under several flow simulation processes with four different angles of attack starting from 0° and increasing in increments of 2° until 4°.

The rear wing was modelled with the Surfaces tool available for use in SolidWorks CAD (Computer Aided Design) software and all surfaces have been knitted together in order to obtain a completely solid structure for better flow analysis. The wing design consists of two side sections and a middle section, all following the S1223 aerofoil profile however with different cord lengths: the side sections have got a cord length of 558.8 mm (22 in) and the middle part which the main downforce generating section has got a chord length of 457.2 mm (18 in). The idea behind keeping the chord length of the side sections longer than that of the middle section was to provide the air flow with more surface area to flow and minimise wake regions which arise as a result of

flow separation. The chord length was kept the same for all three different angles of attack.

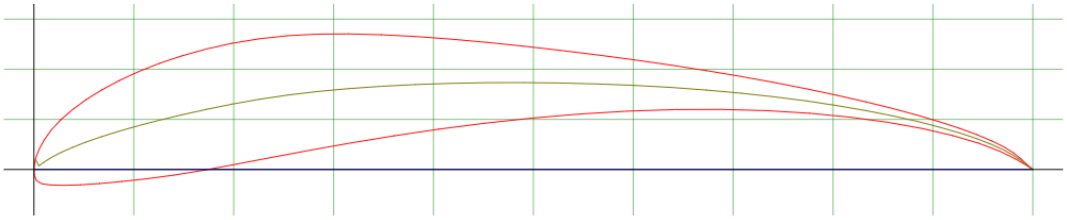

Figure 5: S1223 aerofoil profile: specialised for high lift and low Reynolds numbers.

(a)

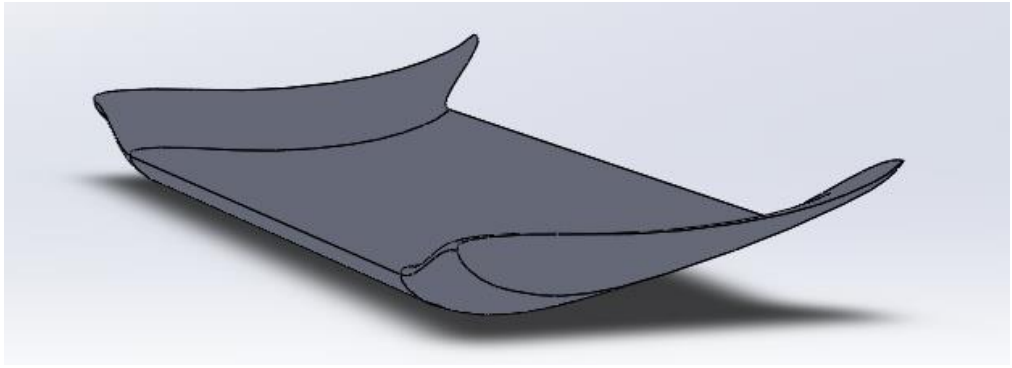

(b)

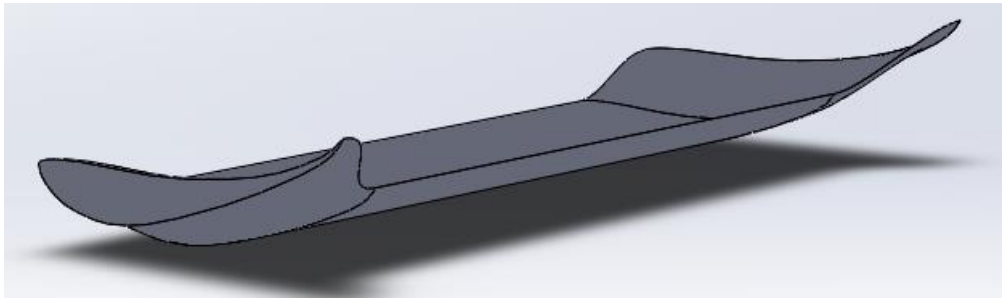

Figure 6: (a), (b); Rear wing design with S1223 aerofoil profile.

3.2 CFD Simulation

The CFD simulations were performed using ANSYS Fluent software. As simulating turbulent flow over the rear wing design would have been much more suitable when it comes to simulating real life situations, standard k-ε two equation model turbulent flow model was utilised.

The limitations of the standard k-ε turbulence model are mainly listed as; no-slip walls, adverse pressure gradients, and simulating flow over strong curvatures. Difficulty of solving epsilon is another major limitation however it can be eliminated by choosing the correct convergence criteria. On the other, recent scientific research which investigated different kinds of k-ε model have showed that the standard k-ε two equation model provides satisfactory results.

Moen et al. investigated the performance of three major Reynolds averaged Navier-Stokes (RANS) turbulence models; standard k-ε, Reynolds normalization group (RNG) k-ε, and realisable (RKE) k-ε model. These turbulence models were tested in terms of accuracy to experimental data. Moen et al. stated that the standard and RNG k-ε models provided satisfactory results and validation to experimental data on other literature. Additionally, it was mentioned that the RKE k-ε model was the most successful for complex geometries [17].

Since the rear wing design investigated in this study is not a highly complex geometry, it was decided that it would be suitable to utilise standard k-ε model.

3.2.1 Simulating the Wind Tunnel Environment

In order to simulate a wind tunnel test, the rear wing geometry was placed in enclosure, which has got the dimensions given in Table 2, and the enclosed rear wing can be seen in Figure 14. In addition to this, the solid wing geometry was subtracted from the fluid enclosure which is air surrounding the wing using the Boolean Subtract function of ANSYS Fluent software, in order to effectively simulate the external air flow around the rear wing. This process helped in achieving a fully fluid domain with the shape of the rear wing inside ready for simulation.

The enclosure geometry was not set to be symmetric at all dimensions on purpose. The negative z-axis length behind the trailing edge was set to be longer than the positive z-axis length in front of the leading edge of the wing. The underlining purpose for setting up such an enclosure was that the main area of interest during turbulent flow simulations was the wake region, which happens at the trailing edge of an aerofoil. The negative y-axis length was set to be relatively lower than the positive y-axis length as nothing significant was being suspected to take place at the suction (lower) surface of the wing. The only major factor to be taken account in that case was the pressure difference between the pressure (upper) surface and the suction surface of the wing.

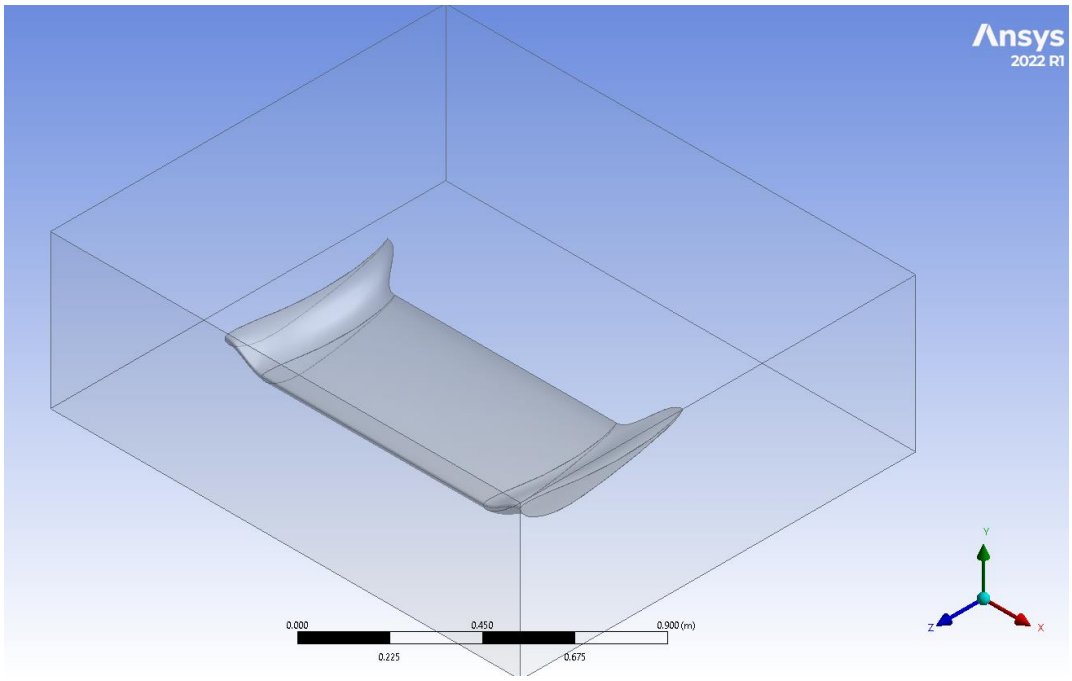

Figure 7: Rear wing in a fluid enclosure.

Table 1: Dimensions of the fluid enclosure around the wing.

Distance (based on the coordinate system)	Length (m)
+X value	0.3
+Y value	0.3
+Z value	0.3
-X value	0.3
-Y value	0.1
-Z value	0.5

3.2.2 Mesh Structure

Tetrahedral elements were utilised for mesh creating as they are more suitable for capturing data during air flow. In order to keep the computation time to a minimum, the mesh of the air domain was kept coarser up to some extent when compared with the mesh structure generated on the rear wing. The mesh generated for the air domain surrounding the wing was specified to be for purposes of fluid dynamics study just to keep more reliability throughout the simulation process and prevent errors as much possible. The mesh structure can be observed clearly in the Figures 15 – 20. Table 2

displays numerical information on the mesh, which was adjusted as default by the ANSYS Fluent software around the wing.

Table 2: Mesh information.

Nodes	Elements	Minimum Element Size (m)	Maximum Element Size (m)
95865	527195	0.10859	0.21719

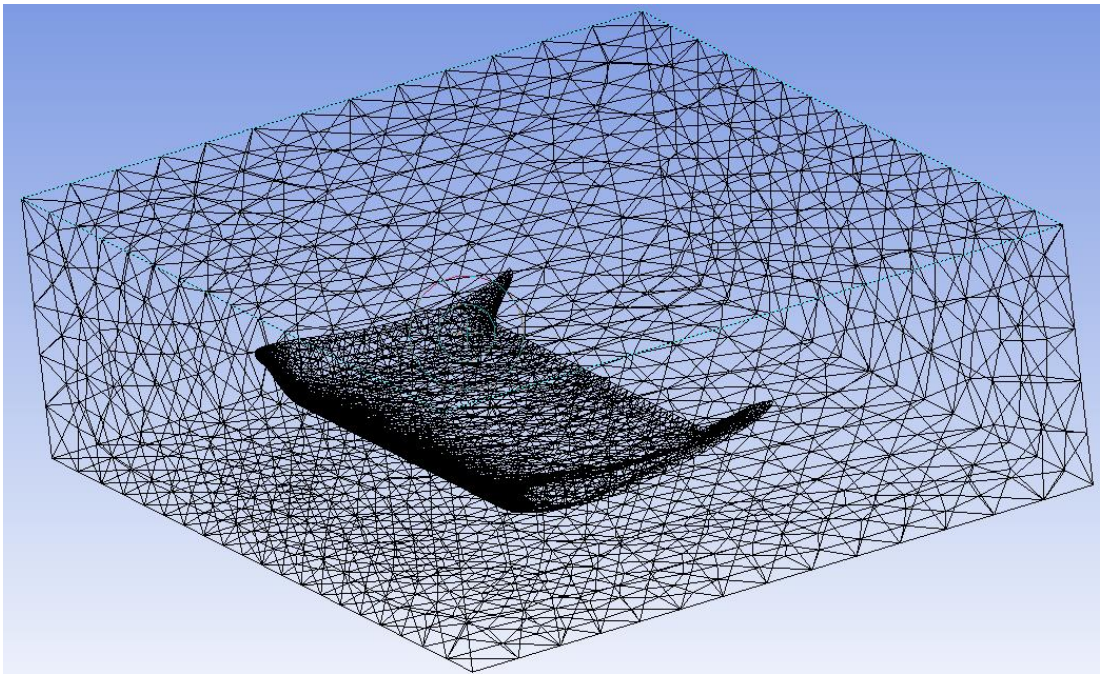

Figure 8: Mesh structure on the fluid domain and the rear wing.

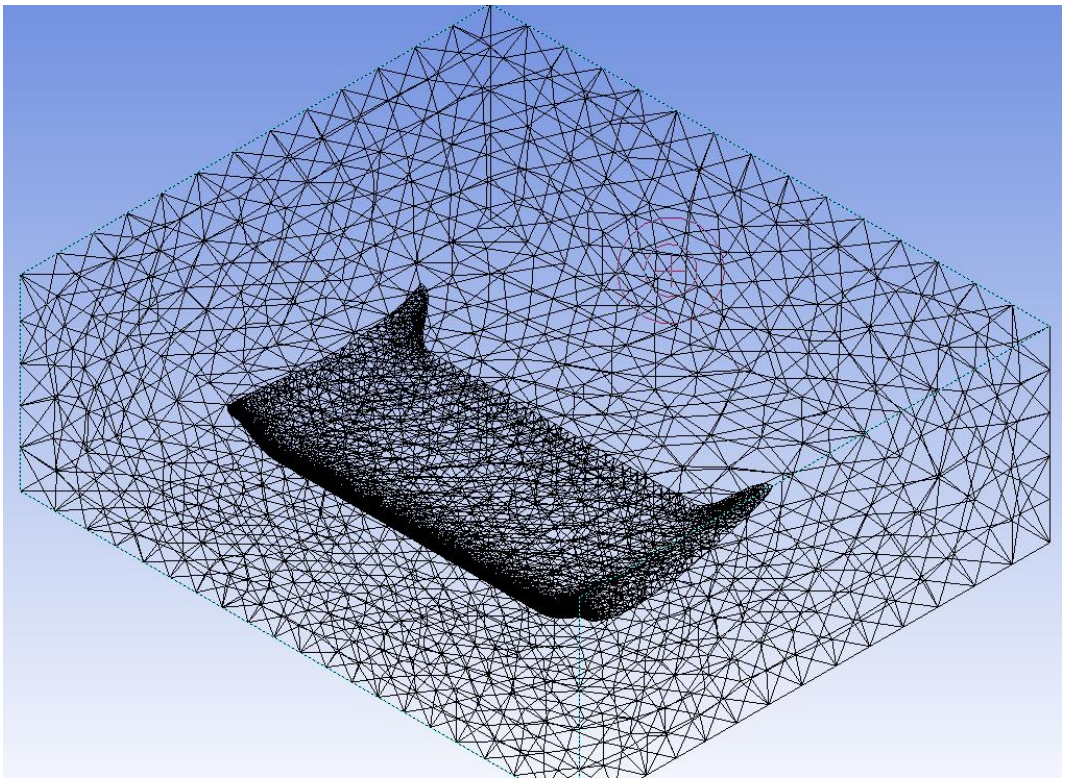

Figure 9: Mesh structure on the fluid domain and the rear wing from a higher point of view.

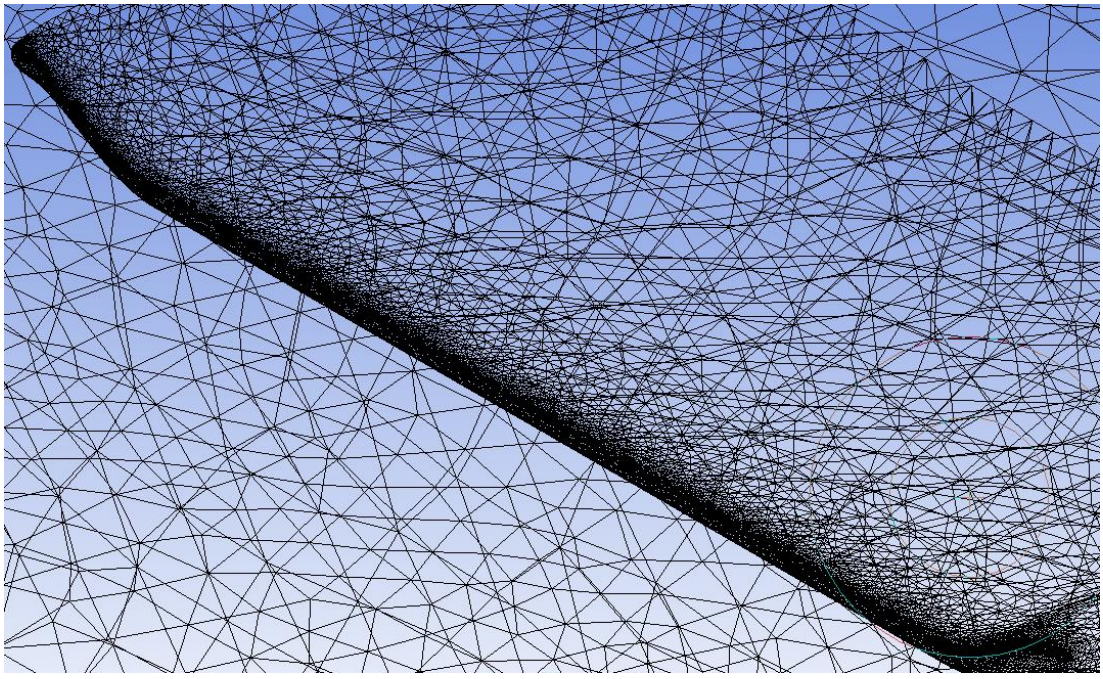

Figure 10: Finer mesh on the leading edge of the rear wing.

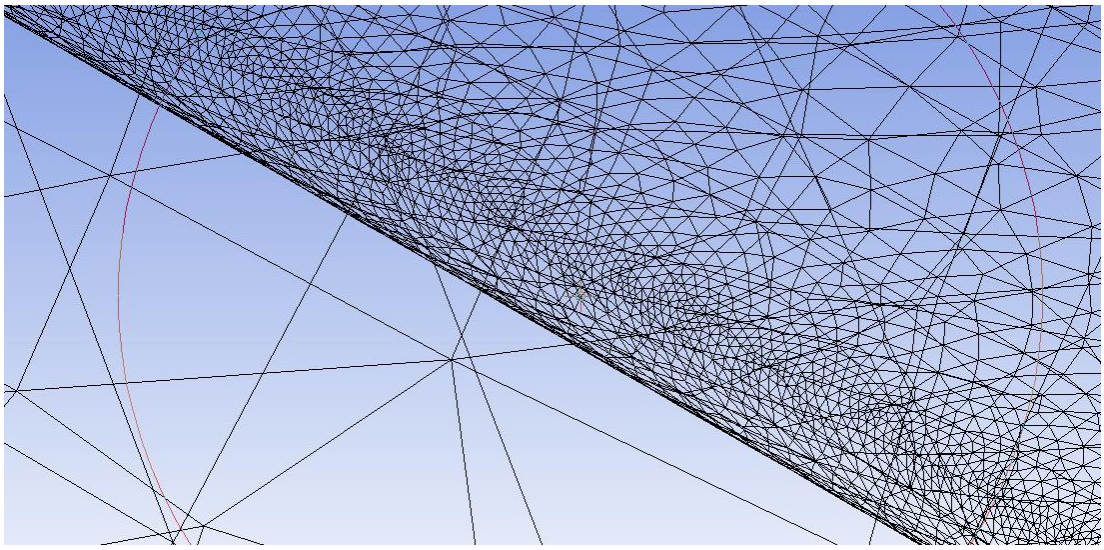

Figure 11: A closer look at the finer mesh on the leading edge of the rear wing.

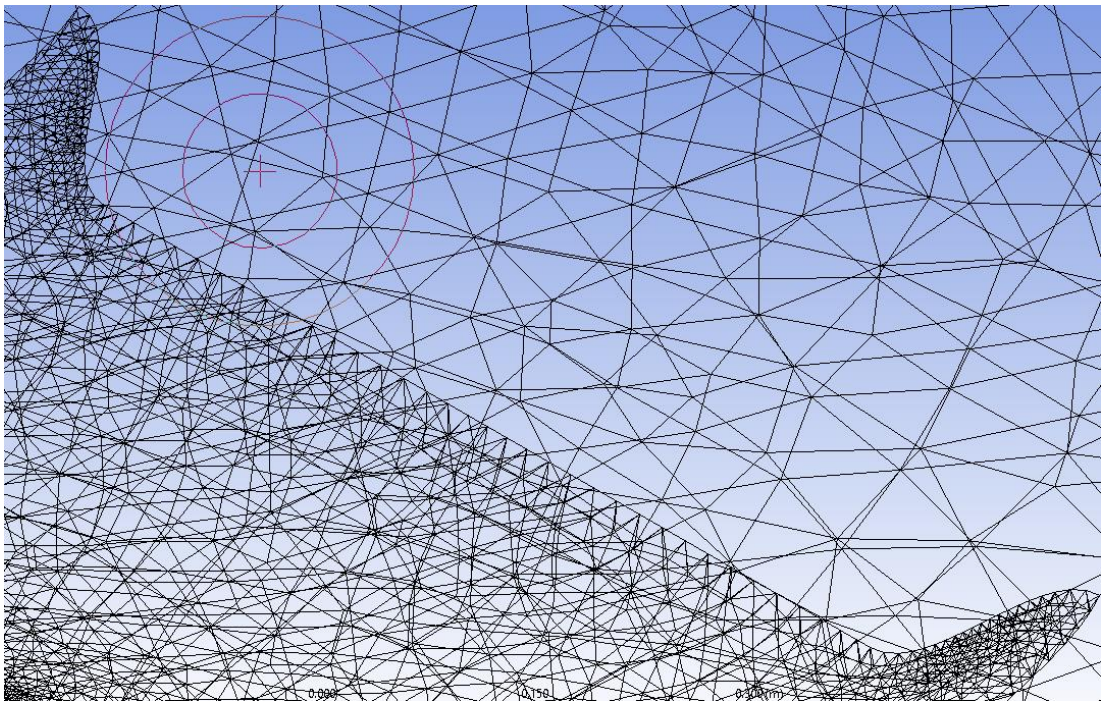

Figure 12: Finer mesh on the trailing edge of the rear wing.

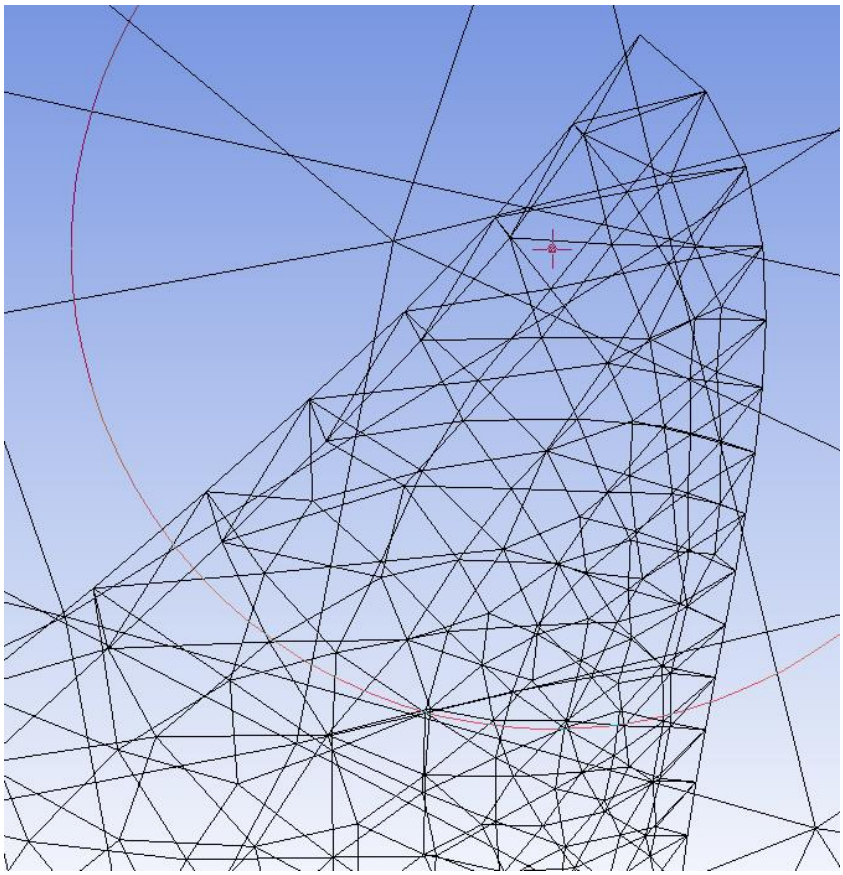

Figure 13: A closer look at the finer mesh on the trailing edge of the rear wing.

3.2.3 Boundary Conditions

One of the major boundary conditions were set to be no-slip condition at the walls. The magnitude of the inlet velocity was set to be 20 m/s for all three angles of attack, where the outlet was set to be a pressure outlet to discharge at atmospheric pressure. The turbulence intensity at the inlet was set by default to be 5%, which was suitable for external flow over vehicle bodies and parts and as well as low Reynolds number flows, in which the S1223 aerofoil was specialised. Additionally, the turbulent viscosity ratio (ratio between turbulent viscosity and dynamic viscosity) was set to be 10. These boundary conditions can be observed clearly in Table 3. Additionally, the inlet and outlet flow can be seen observed in Figure 15.

European naturalistic driving data and recent research have displayed the driving speeds on highways in major European countries. It was shown that an ordinary driver has the potential to interact with secondary tasks such as texting when driving demand is low on the highway. This will result in reducing the travelling speed below the national highway speed limit, which is 100 km/h in major European highways. Additionally considering the congested modern traffic, European driving data suggested that the approximate driving cycle for on the European highways is between 80 – 100 km/h, which roughly translates to 20 – 30 m/s [18], [19].

Based on that information, the above-mentioned travelling speeds were decided as a decent candidate for flow velocity in this study.

Table 3: Flow and turbulence boundary conditions.

Flow Boundary Condition	**Type**	**Value**
Inlet	Velocity	20 - 30m/s
Outlet	Pressure	Atm
Turbulence Boundary Conditions		
Turbulence Intensity		5%
Turbulence Viscosity Ratio (μ_t/μ)		10

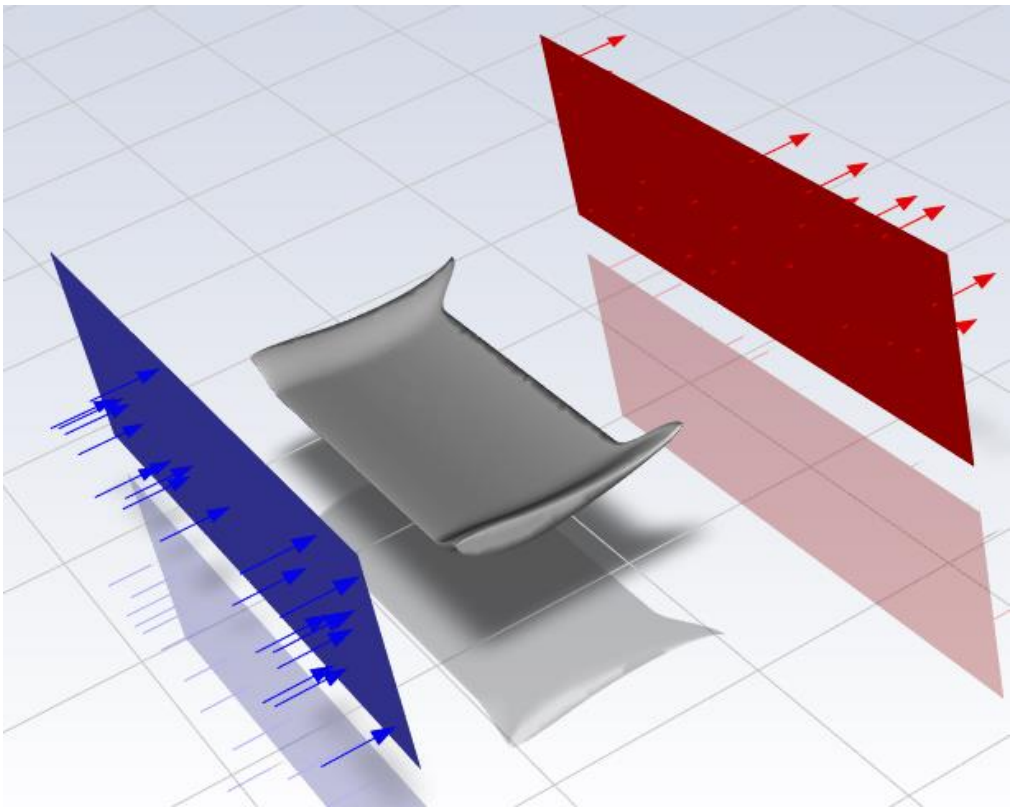

Figure 14: Inlet and outlet air flow illustration.

Since the purpose of the simulation was to simulate turbulent flow over the wing, further flow variables about the turbulent behaviour of the flow were calculated by the ANSYS fluent software and specified; these variables can be observed in Table 4. X, Y, and Z components of the velocities; based on the coordinate system on Figure 14, can also be seen from Table 4, where X and Y velocity components were set to be infinitesimally small but never zero.

Table 4: All three velocity components and turbulence variables.

Variable	**Value**
X velocity	-7.84112e-20 m/s
Y velocity	7.41011e-17 m/s
Z velocity	-20 m/s
Turbulence Kinetic Energy (k)	1.5 m^2/s^2
Turbulence Dissipation Rate (ε)	1386.289 m^2/s^2

The k-ε turbulence model constants were also provided in the ANSYS fluent software and these can be observed in Table 5.

Table 5: Standard k-ε turbulence model constants.

Turbulence Model Constant	**Value**
$C\mu$	0.09
$C\varepsilon_1$	1.44
$C\varepsilon_2$	1.92
k Turbulence Kinetic Energy	1
ε Turbulence Dissipation Rate	1.3

Chapter 4

RESULTS AND DISCUSSION

4.1 Residuals

In order to prevent the simulation from converging before reaching the target of 100 iterations, all the residuals were set not to converge during the computation process. This increased the dependability of the simulation up to an extent and the residuals were observed to be decreased throughout 100 iterations as expected. The residuals graphs for all three simulations with three different angles of attack have been provided in Figures 22 – 24. The Reynolds Number was calculated to be Re = 555×10^3 as the flow was passing over the chord of the wing. This value suggests that the flow was turbulent as it was passing around the wing, which was expected from this study.

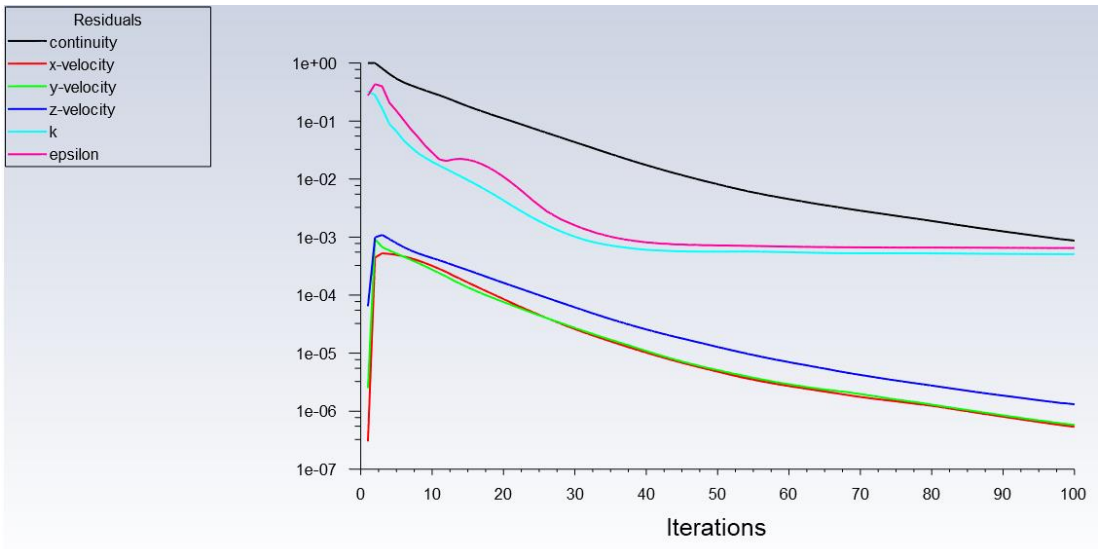

Figure 15: Residuals of the simulation of rear wing with 0° angle of attack.

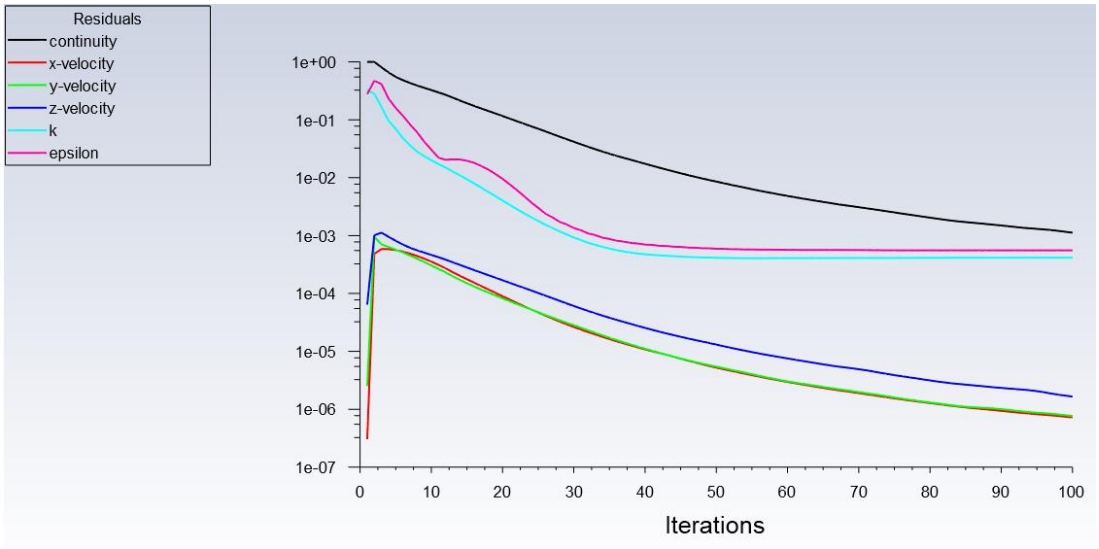

Figure 16: Residuals of the simulation of rear wing with 2° angle of attack.

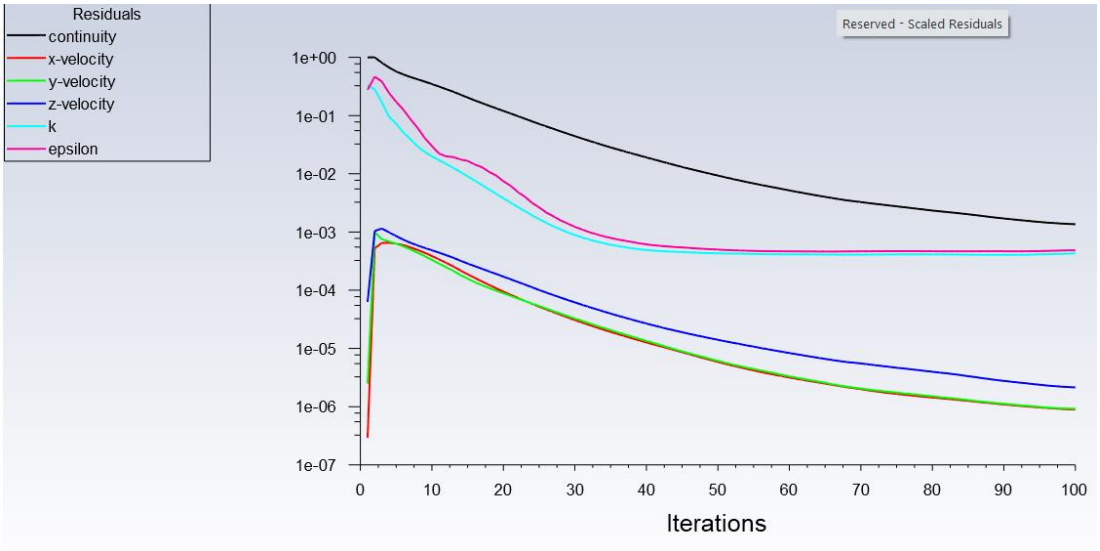

Figure 17: Residuals of the simulation of rear wing with 4° angle of attack.

4.2 Flow Visualisation

Flow visualisation was performed on the wing as a post-processing step. Velocity and pressure contours, vectors, and streamlines were visualised on the mid plane of the rear wing in 2D YZ-plane, where the wing design is symmetric. However, the streamlines were also visualised in 3D to clearly observe the flow around the wing and the eddies on the trailing edge. A total of 110 contours were used for velocity and pressure contours, and 200 streamlines were made visible. The plane where the flow was visualised, together with the reference coordinate system, can be seen in Figure 25.

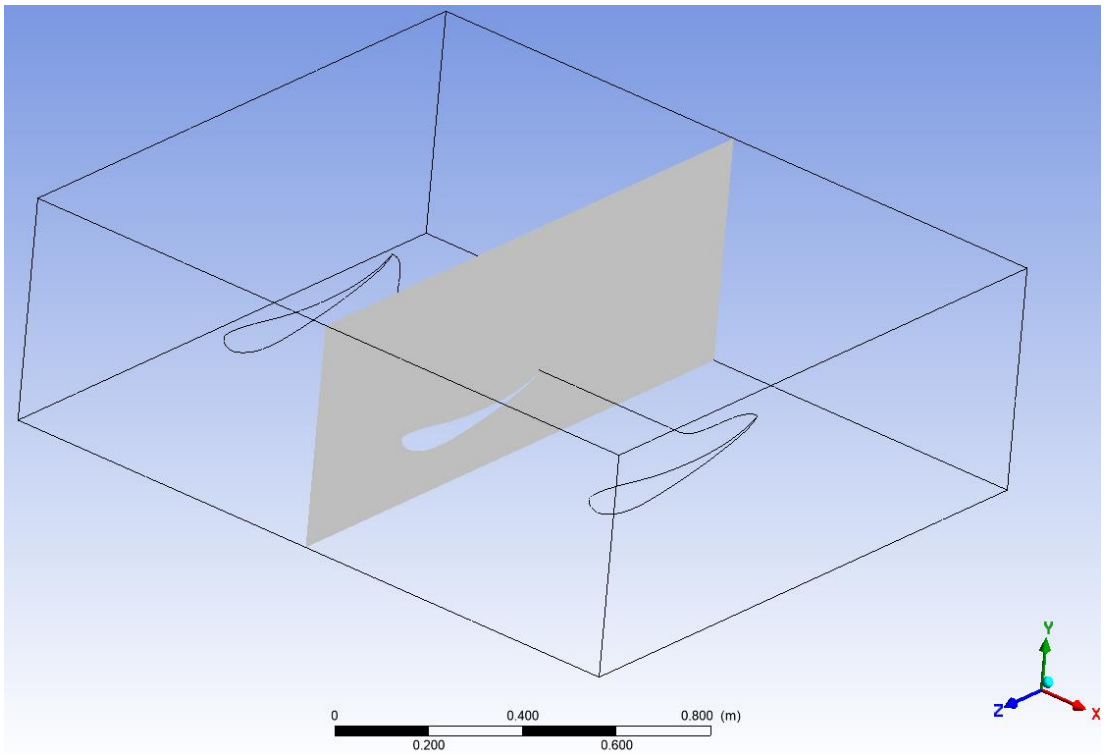

Figure 18: The plane where the flow was visualised on.

4.2.1 Flow Visualisation on the Wing at 0° Angle of Attack

The velocity and pressure contours of the wing displayed satisfactory results, where the aerofoil was successful in slowing the air flow on the pressure and suction surfaces of the wing. Moreover, a negative pressure was present beneath the suction surface of the wing as expected, contributing to the downforce enhancement by introducing suction. Visualised flow for the 0° angle of attack wing can be seen in Figures 26 – 31.

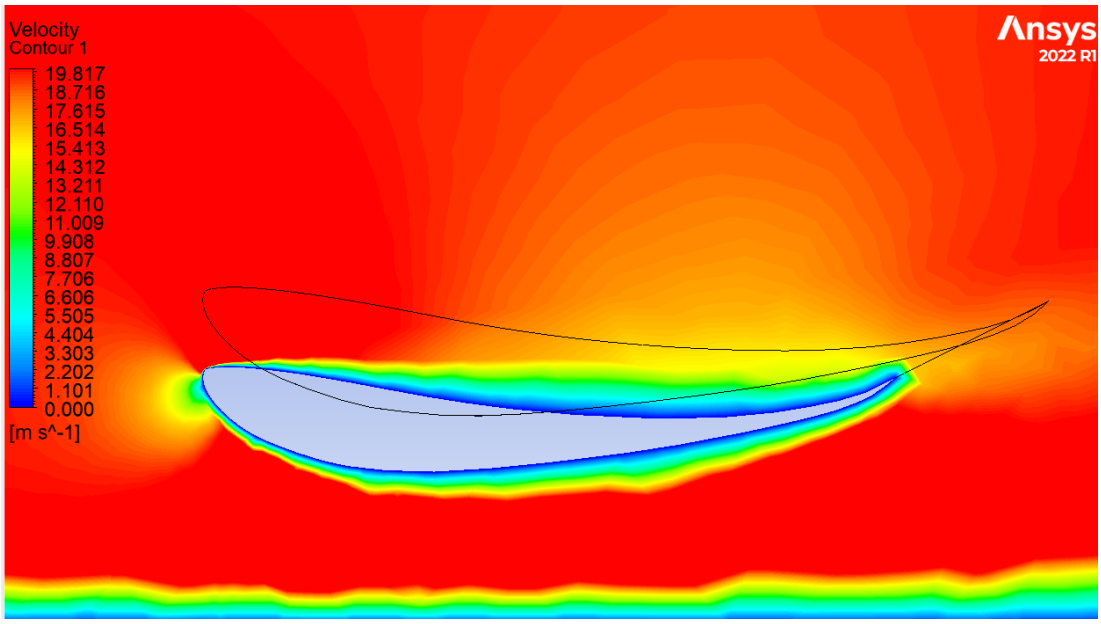

Figure 19:Velocity contour of the wing at 0° angle of attack.

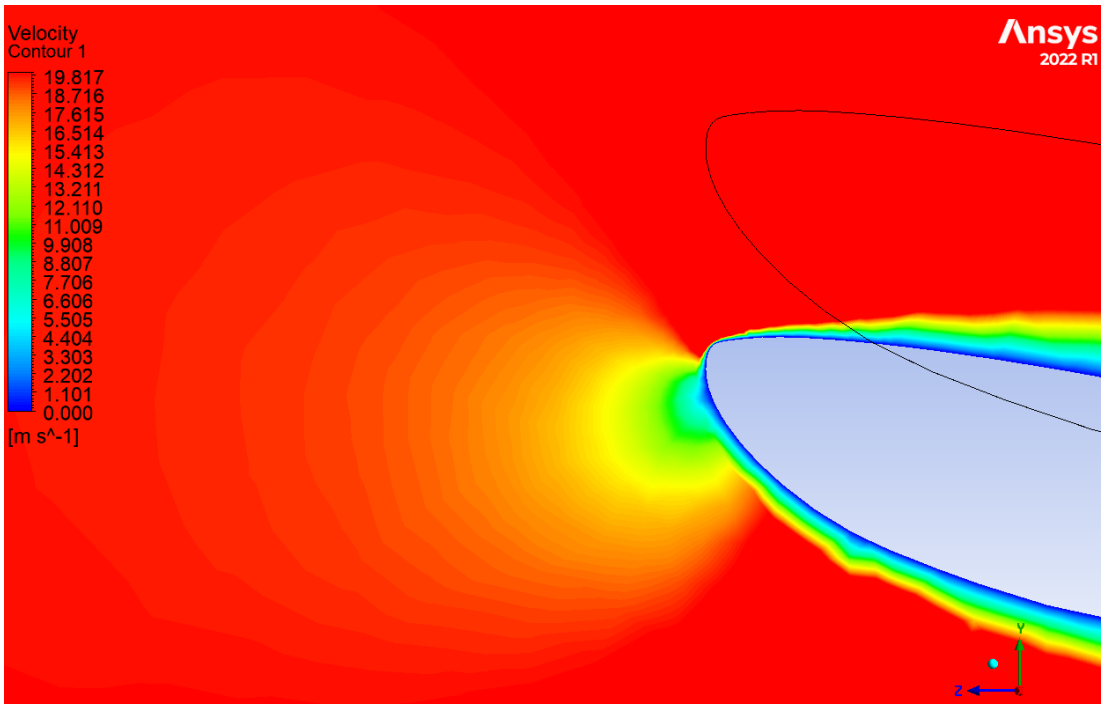

Figure 20: Stagnation point on the leading edge of the wing at 0° angle of attack.

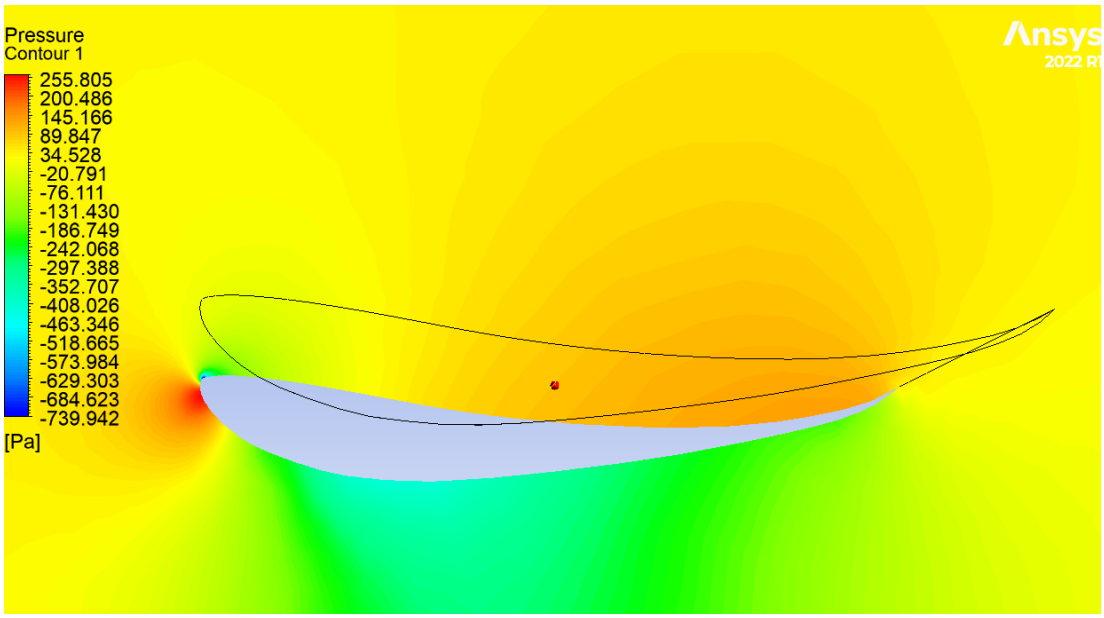

Figure 21: Pressure contour of the wing at 0° angle of attack.

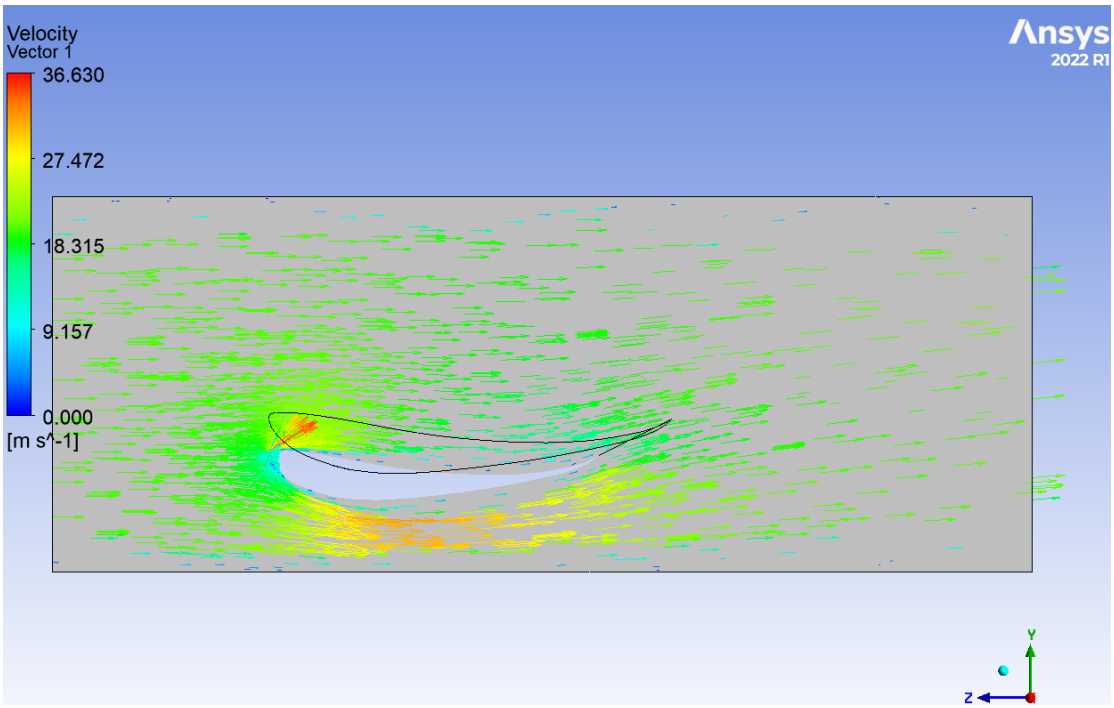

Figure 22: Velocity vectors of the wing at 0° angle of attack.

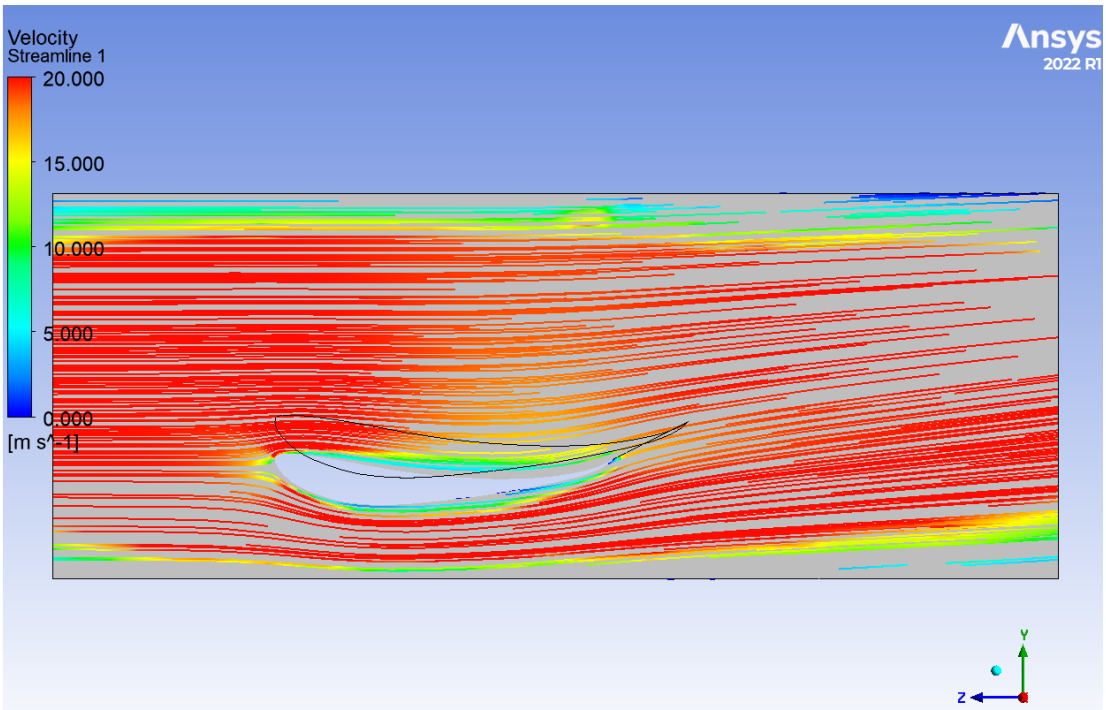

Figure 23: Streamlines on the middle plane of the wing at 0° angle of attack.

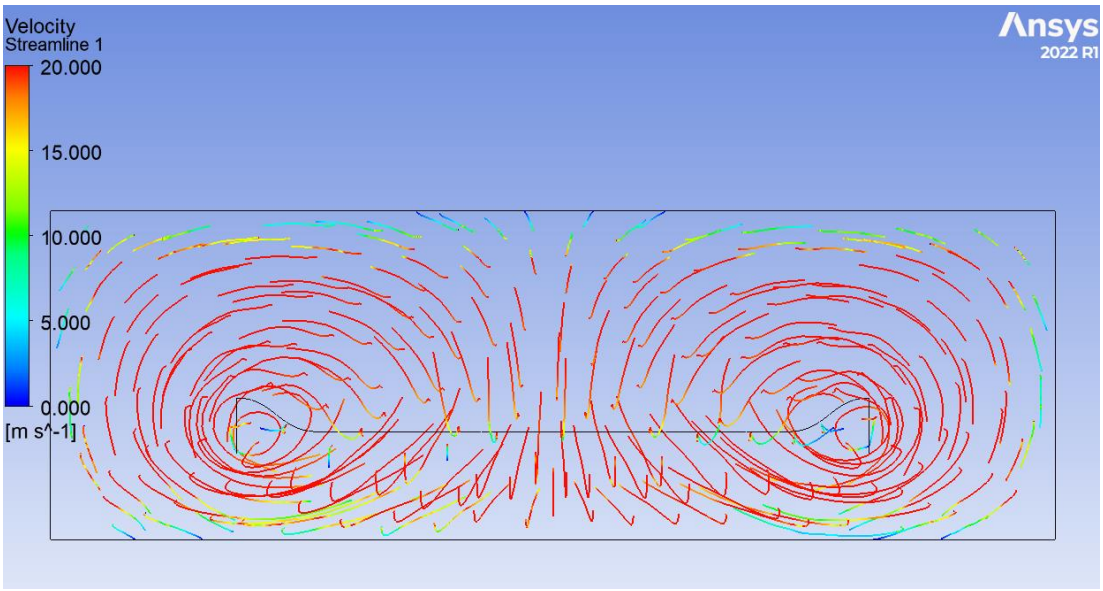

Figure 24: Streamlines at the trailing edge of the wing at 0° angle of attack.

4.2.2 Flow Visualisation on the Wing at 2° Angle of Attack

Visualised flow on the wing at 2° angle of attack showed similar behaviour to that of 0° angle of attack. The aerofoil profile was once again proven to be efficient in slowing down the air flow on the pressure and suction surfaces of the wing. A negative pressure zone was also generated beneath suction surface of the wing. The flow visualisation data at 2° angle of attack can be observed in Figures 32 – 37.

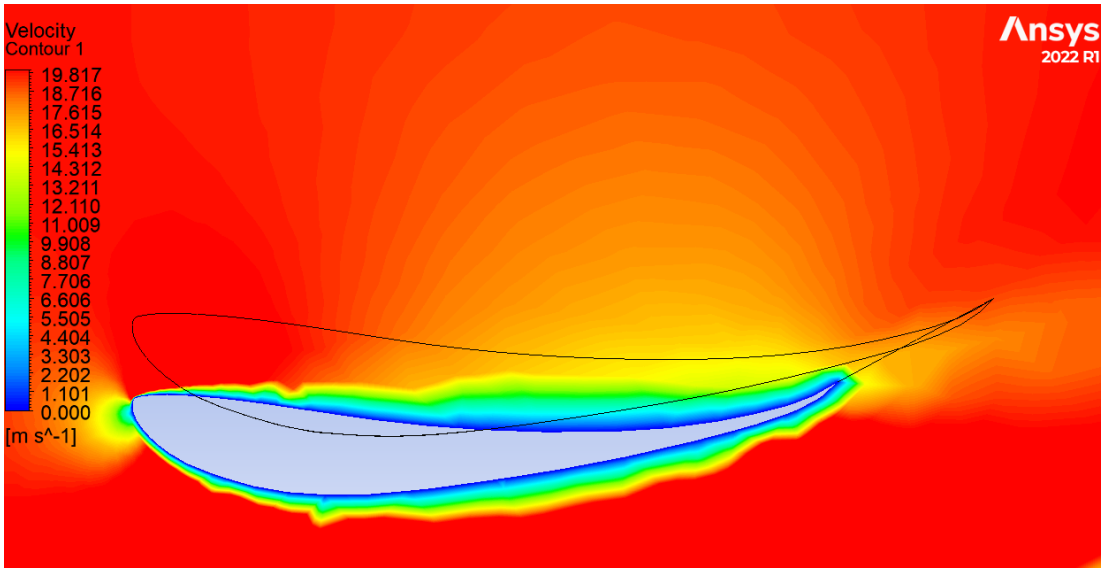

Figure 25: Velocity contour of the wing at 2° angle of attack.

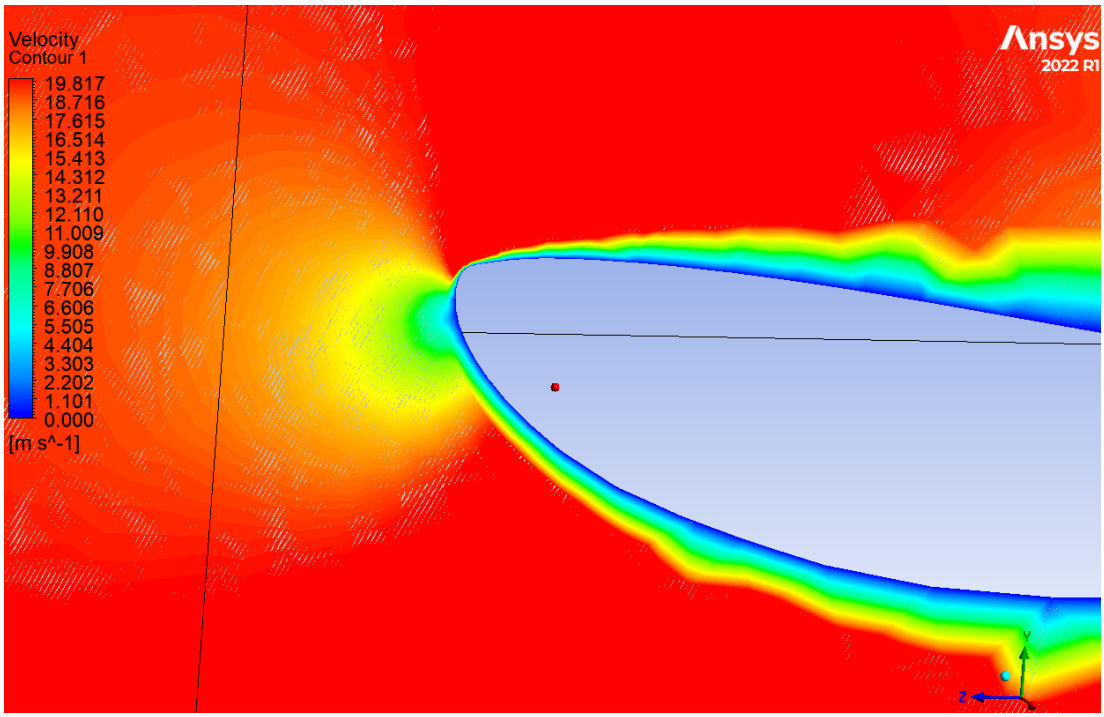

Figure 26: Stagnation point on the leading edge of the wing at 2° angle of attack.

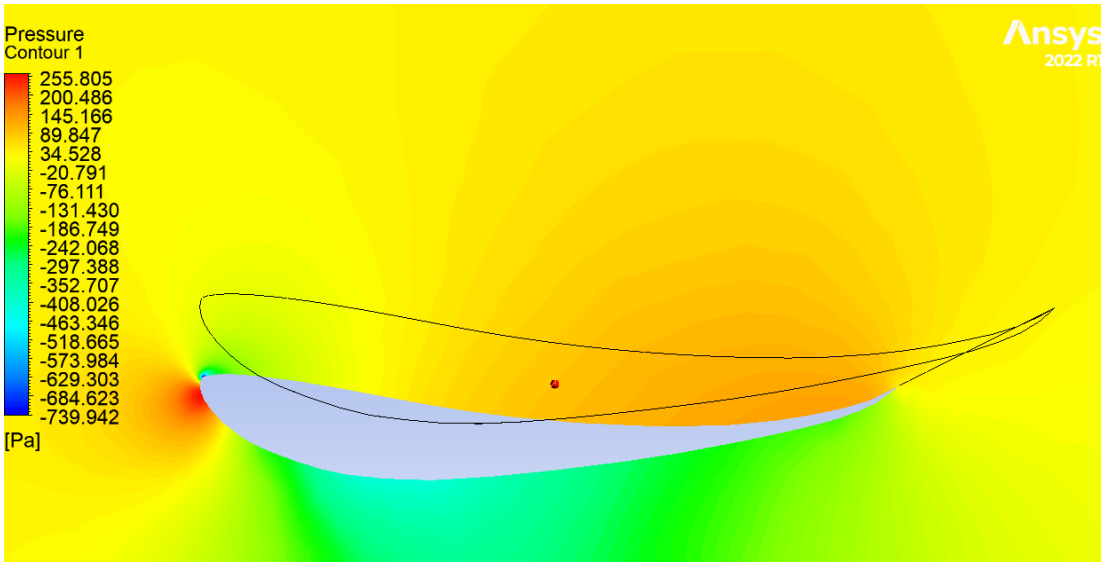

Figure 27: Pressure contour of the wing at 2° angle of attack.

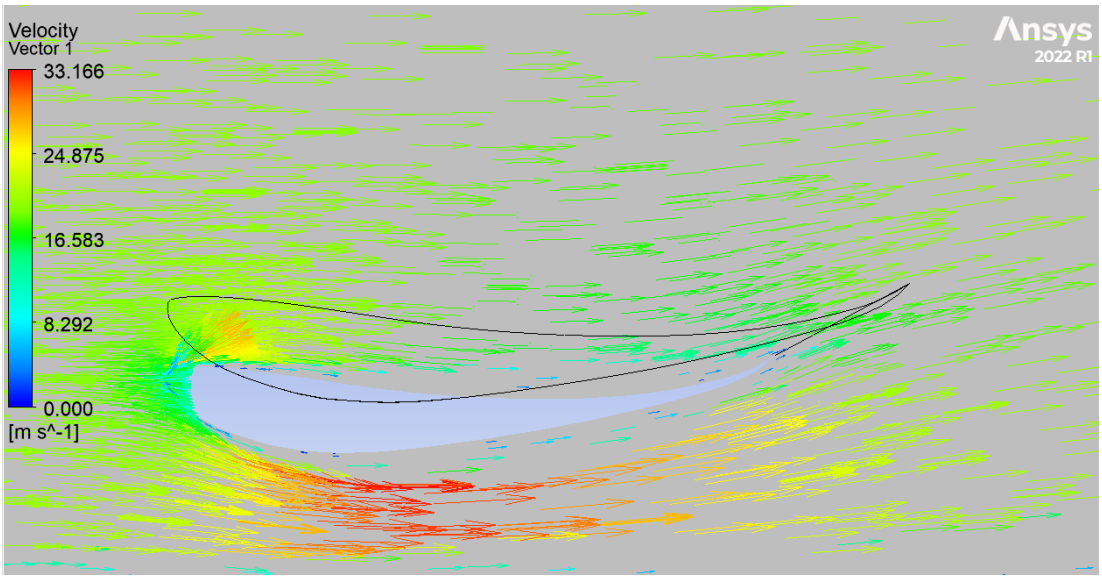

Figure 28: Velocity vectors of the wing at 2° angle of attack.

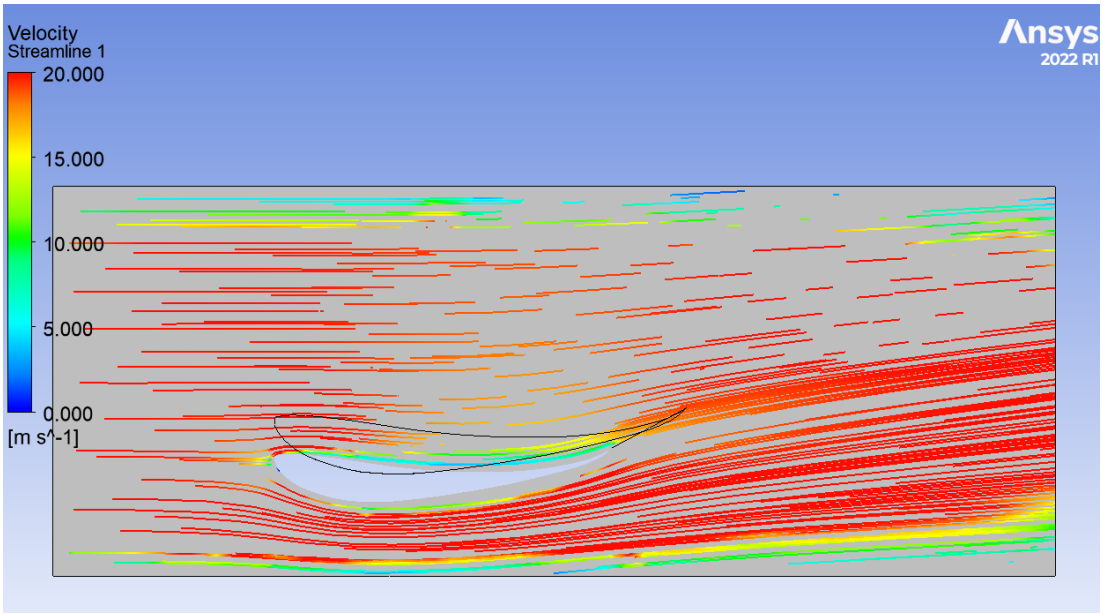

Figure 29: Streamlines on the middle plane of the wing at 2° angle of attack.

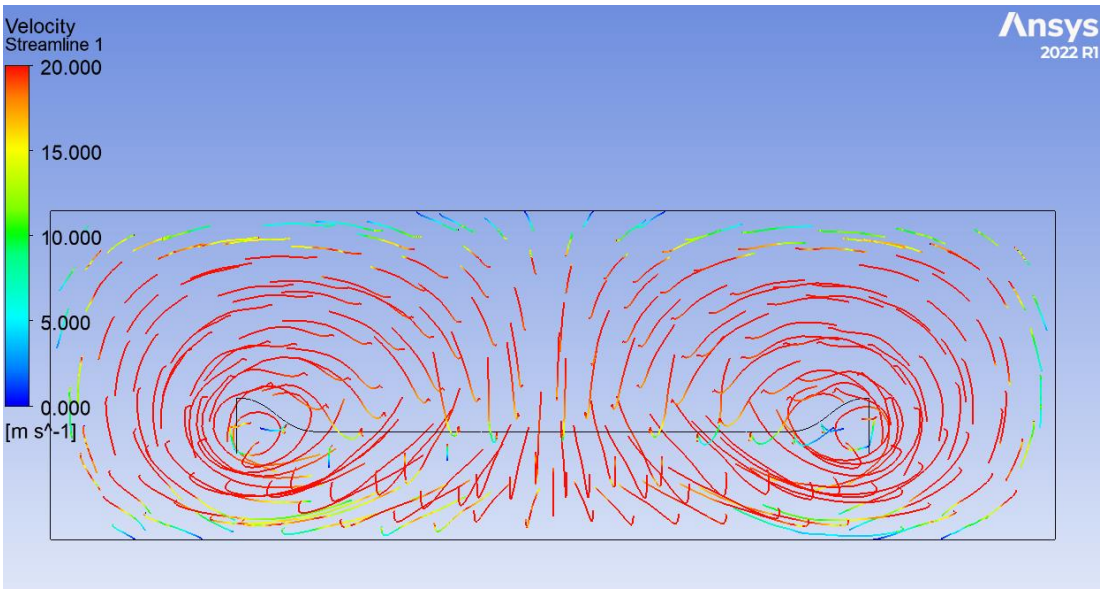

Figure 30: Streamlines at the trailing edge of the wing at 2° angle of attack.

4.2.3 Flow Visualisation on the Wing at 4° Angle of Attack

It is safe to mention that consistency was kept throughout the simulation since the higher angle of attack of 4° displayed similar behaviour as the previous two settings. Air flow was slowed down successfully by the aerofoil on the pressure and suction surfaces, with a lower pressure zone underneath the wing. Visualised flow around the wing at 4° angle of attack can be seen in Figures 38 – 43.

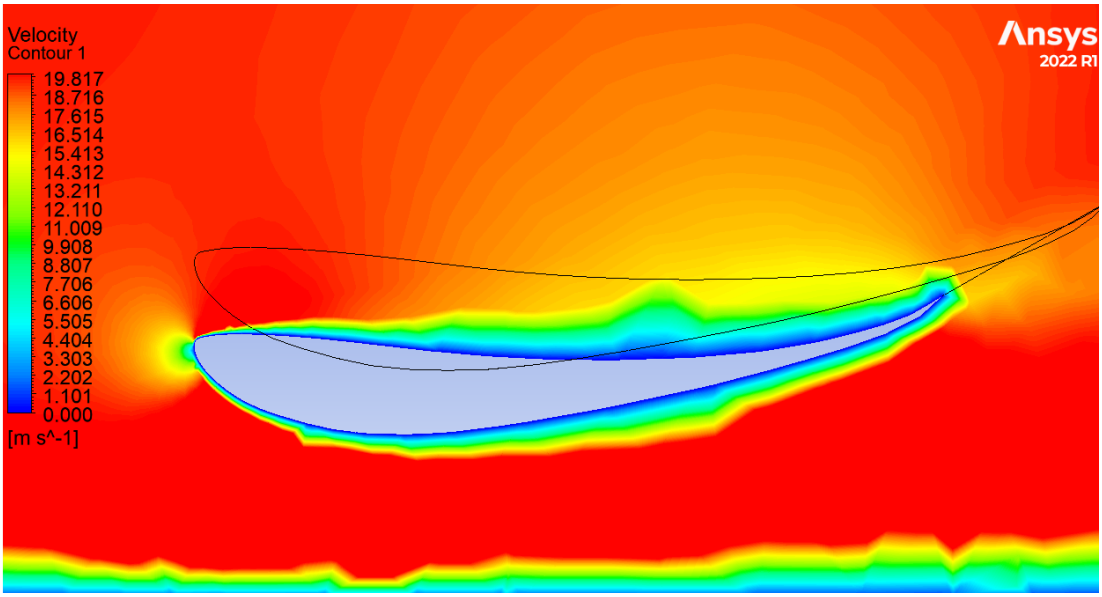

Figure 31: Velocity contour of the wing at 4° angle of attack.

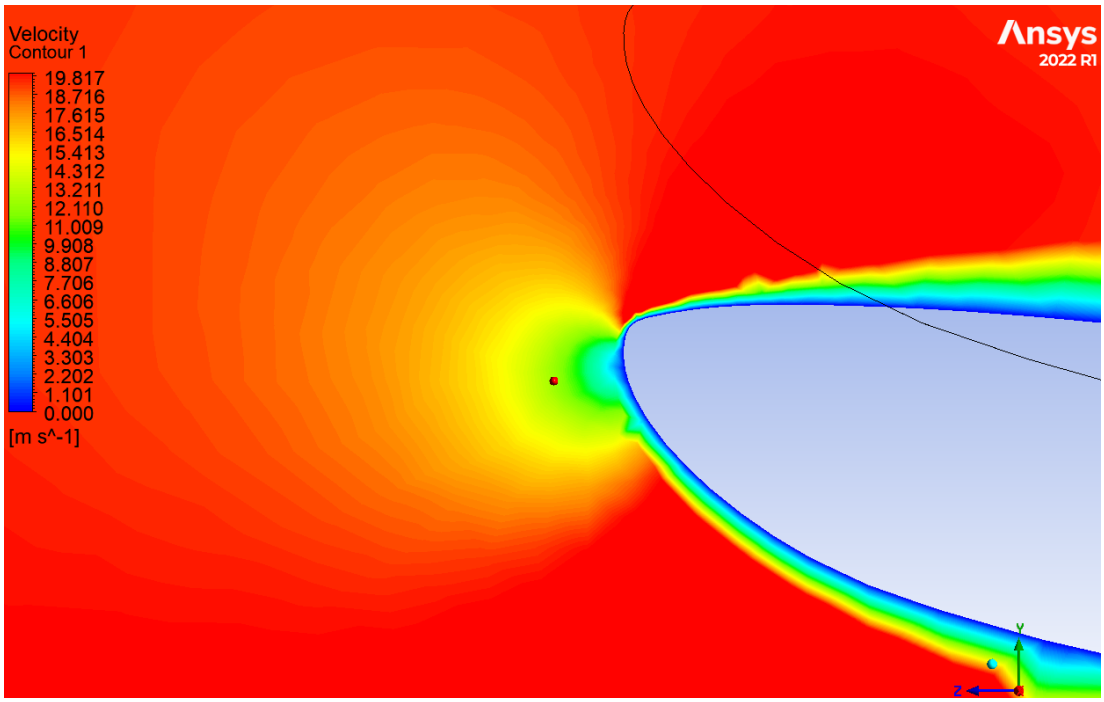

Figure 32: Stagnation point on the leading edge of the wing at 4° angle of attack.

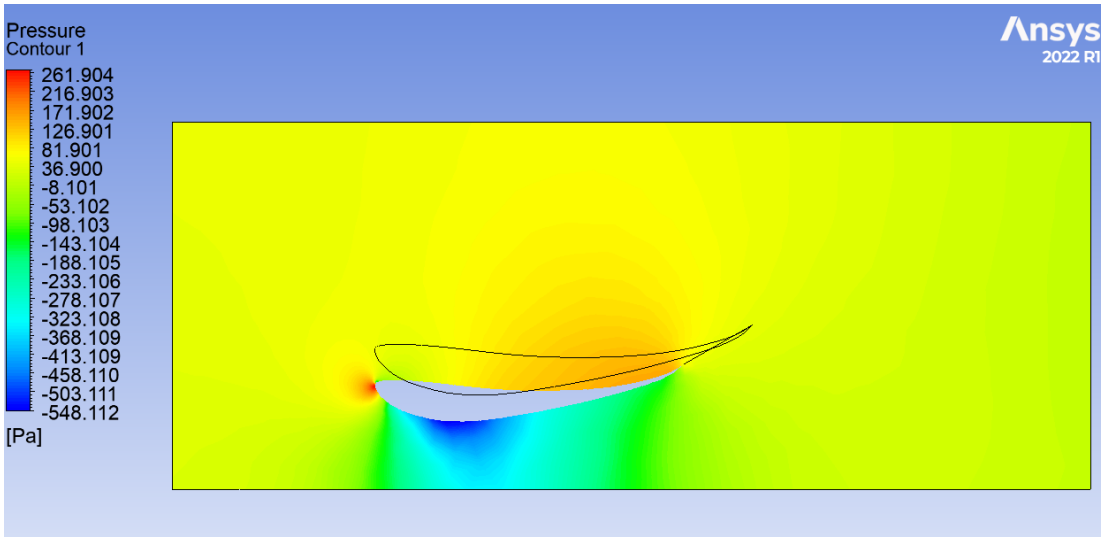

Figure 33: Pressure contour of the wing at 4° angle of attack.

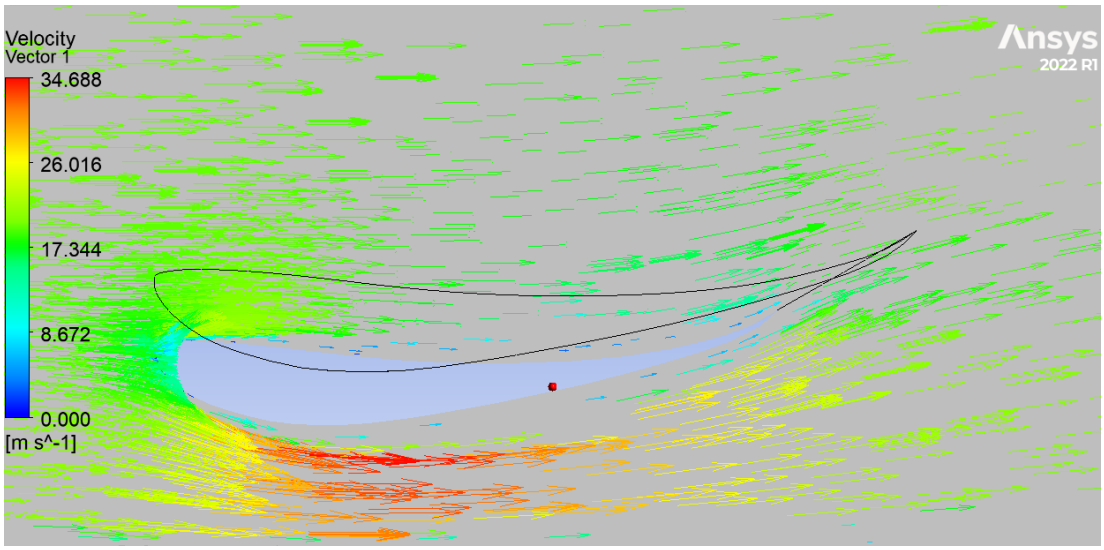

Figure 34: Velocity vectors of the wing at 4° angle of attack.

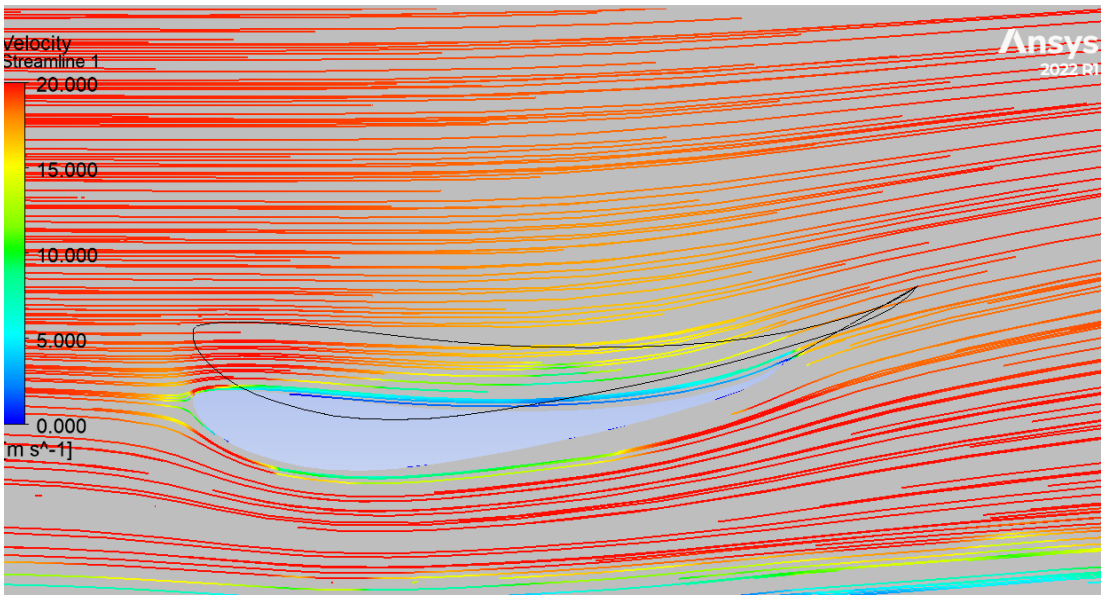

Figure 35: Streamlines on the middle plane of the wing at 4° angle of attack.

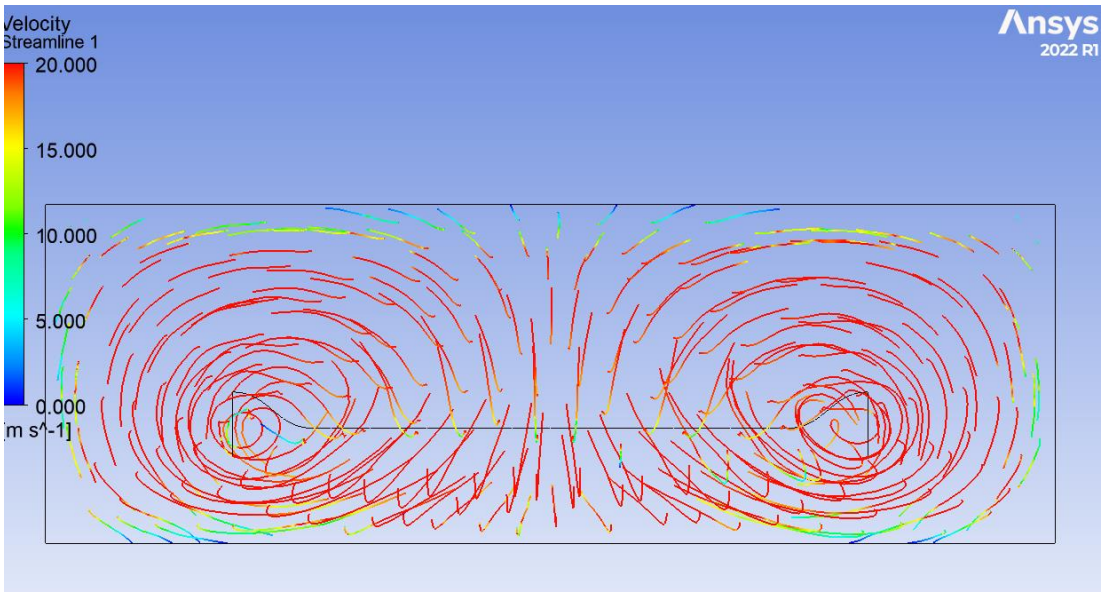

Figure 36: Streamlines at the trailing edge of the wing at 4° angle of attack.

4.3 Downforce and Drag Force

Downforce and drag force generated on the wing were calculated using the ANSYS software. Three sets of calculations at three different angles of attack were performed based on the forces exerted on the wing in Y-axis (downforce) and Z-axis (drag force). The Y-axis measurements were found to be negative values meaning that negative lift; hence downforce, was generated by the wing. The calculated downforce, D, frag force, F_D, and downforce to drag ration, D/F_D together with the force coefficients can be seen in Table 6.

Table 6: Downforce and drag force data calculated at three different angles of attack.

Angle of Attack	**Downforce (D)**	**Drag Force (F_D)**	**D/F_D**	**Downforce Coefficient (C_L)**	**Drag Force Coefficient (C_d)**
0°	121.891 N	12.895 N	9.5	0.471	0.0499
2°	141.787 N	15.897 N	8.9	0.548	0.0614
4°	161.253 N	19.518 N	8.3	0.623	0.0755

4.4 Negative Angle of Attack

In order to obtain further information on the behaviour of the wing, it was additionally tested at a negative 4° angle of attack, where the wing was basically tilted above the horizontal line. The inlet velocity was set to be 30 m/s however all other flow conditions were kept the same as before. The wing was expected to generate lift, however interesting results were obtained. Flow visualisation data can be seen in Figures 37 – 40, additionally Table 7 displays force calculation at negative angle of attack.

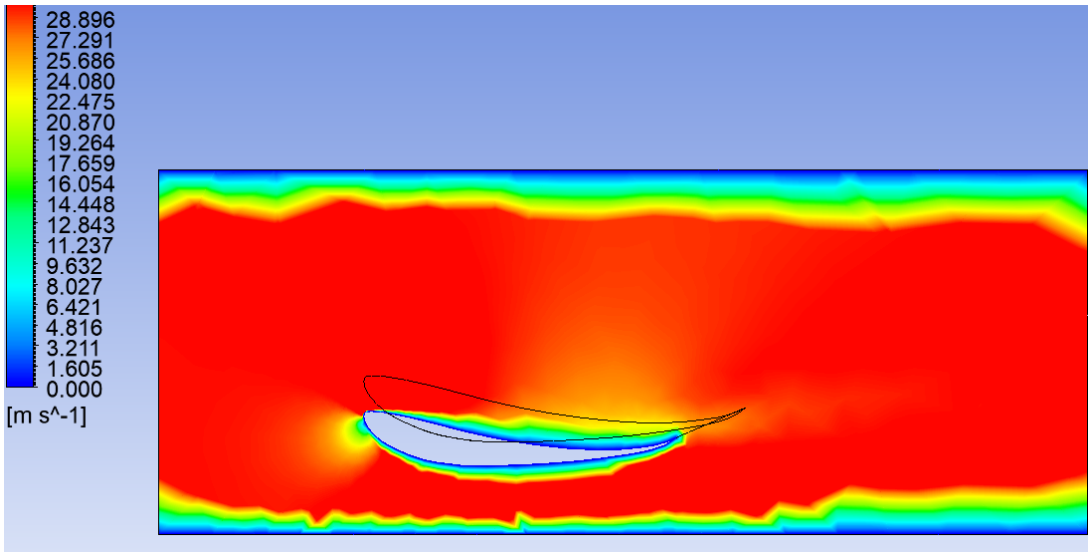

Figure 37: Velocity vector of the wing at negative 4° angle of attack.

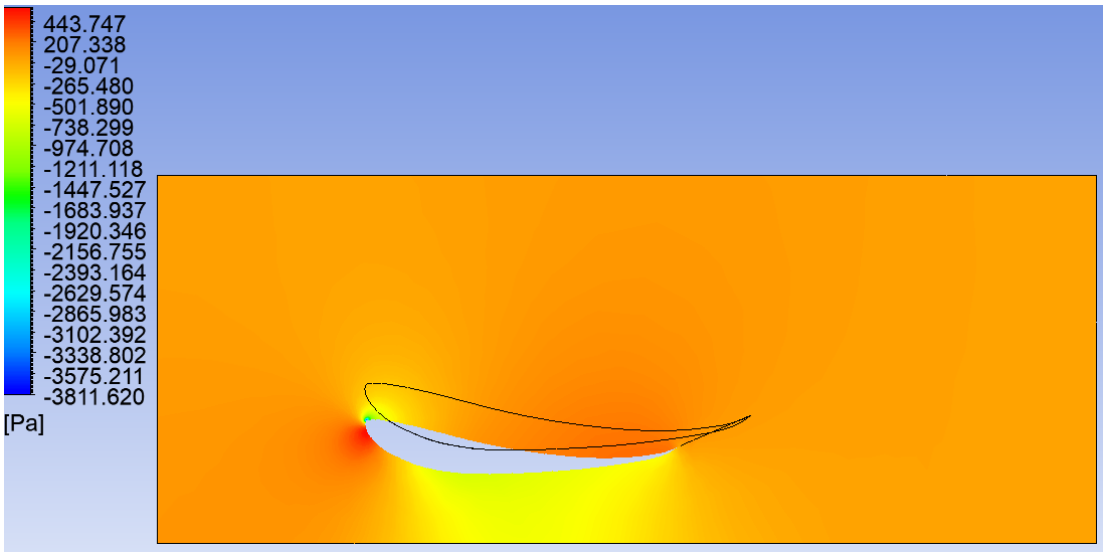

Figure 38: Pressure contour of the wing at negative 4° angle of attack.

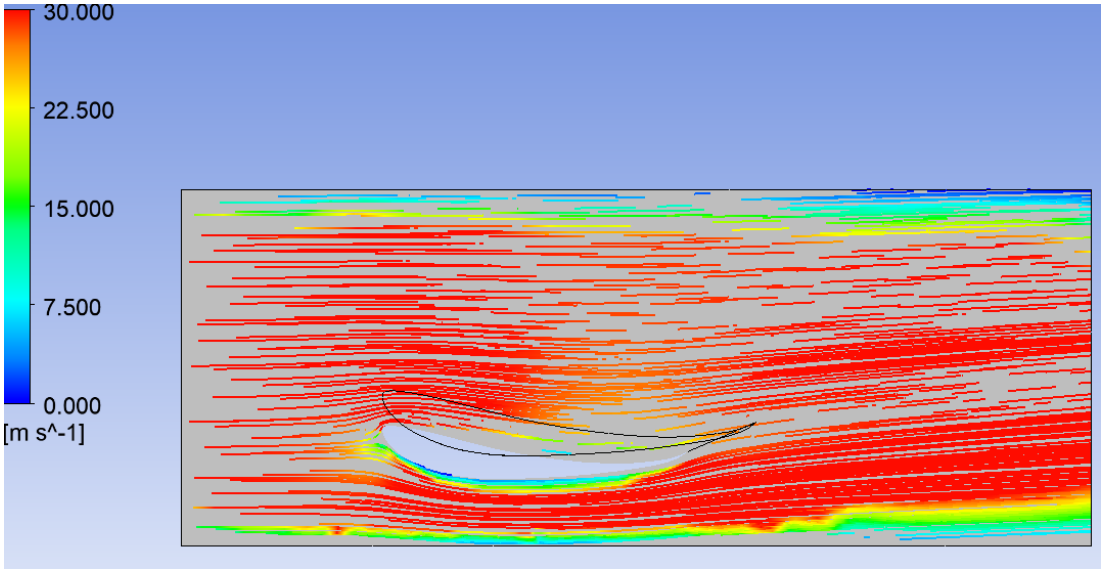

Figure 39: Streamlines on the middle plane of the wing at negative 4° angle of attack.

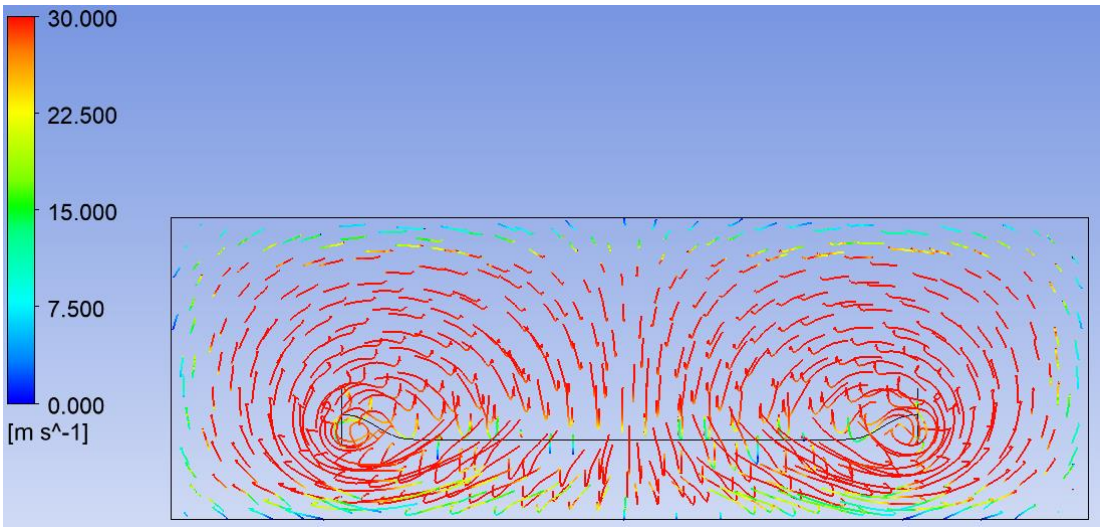

Figure 40: Streamlines at the trailing edge of the wing at negative 4° angle of attack.

Table 7: Downforce and drag force data calculated at negative 4° angle of attack.

Angle of Attack	Downforce (D)	Drag Force (F_D)	D/F_D	Downforce Coefficient (C_L)	Drag Force Coefficient (C_d)
-4°	190.818 N	18.773 N	10.1	0.328	0.0322

4.5 Discussion

The presented data has been observed and commented on. Overall, the 0° angle of attack setting was the most aerodynamically efficient for daily driving scenarios. The 2° angle showed to be beneficial for high-speed cruising. Whereas the 4° angle of attack produced the most downforce and drag force, but since the aerodynamic efficiency was not extremely lower than 2° angle setting and it generated the most downforce, it would be a suitable option for track applications.

In order to obtain further validation, the numerical data obtained from this study were compared with the numerical data obtained by Kurec et al. when their wing was set at low angles of attack (1° and 5°) and the spoiler at horizontal position for accuracy between results. However, Kurec et al. had chosen to utilise RKE k-ε model, which

acts as a comparison between the standard k-ε model used in this study and the RKE k-ε. The experimental data by Kurec et al. were also compared with the numerical findings and can be observed in Tables 8 – 9 [7].

Table 8: Downforce coefficients compared to scientific literature [7].

Angle of Attack	-4°	0°	2°	4°	1°	5°
Standard k-ε	0.328	0.471	0.548	0.623	-	-
RKE k-ε	-	-	-	-	0.545	0.569
Experimental	-	-	-	-	0.432	0.500

Table 9: Drag force coefficients compared to scientific literature [7].

Angle of Attack	-4°	0°	2°	4°	1°	5°
Standard k-ε	0.0322	0.0499	0.0614	0.0755	-	-
RKE k-ε	-	-	-	-	0.458	0.475
Experimental	-	-	-	-	0.525	0.532

4.5.1 Aerodynamic Performance of the Rear Wing

The simulation process was concluded successfully as the rear wing design met the expectations as of aerodynamic performance. The S1223 aerofoil profile was indeed effective at low Reynolds number flow at relatively low angles of attack.

Additionally, it is safe to say that the S1223 aerofoil profile strongly helped the wing design to generate downforce at 0° angle of attack. This was proven by flow simulation and the downforce calculation at 0° angle of attack can be seen in Table 6 to be 121.891 N. However, downforce generating devices always come together with a certain disadvantage being the drag force. Even though the rear wing was set up horizontally with no effective angle of attack, it still generates drag as it passes through air. The drag force generated by the wing 0° angle of attack was calculated to be 12.8 N.

On the hand, when the benefit of downforce generation at considerably low angle of attack, a slight drag force generation can be negligible especially when this certain wing design is to be used on road legal sports cars. After all, drag force is not generated solely by the aerodynamic parts on a vehicle but also by the car body itself; front end, front wind shield, tyres, side view mirrors, wake region behind the rear end of the car.

It was proven that the S1223 aerofoil profile was also aerodynamically successful at angles of attack higher than 0°. However, as mentioned previously the attack angle of the wing was increased by minimal increments during the investigations of this study. When the angle of attack was increased to 2°, post processing calculations showed that the downforce was increased to 161.253 N, resulting in a 16.3% increase in downforce at the same flow conditions and velocity. Nevertheless, more aggressive attack angle also resulted in higher drag force being generated by the wing; with an increase of 25% the drag force at 2° angle of attack was calculated to be 15.897 N.

It should be noted that the increased downforce at higher attack angles can beneficial for stability and handling at real-life applications on road cars; where the angle of the wing can be controlled by an adaptive system based on the velocity of the vehicle. However, since this investigation was performed by the help of a certain CFD software, real-life scenarios can never be simulated thoroughly, especially when dealing with turbulent flow which happens to chaotic in its nature. In real driving scenarios, there would be side wind acting on the wing effectively disturbing the oncoming air flow and aerodynamic performance. These simulations were performed under strict and steady conditions which are not subjected to sudden changes to the oncoming airflow.

Furthermore, the angle of attack was increased for one more investigation, this time setting up the wing at 4°. The downforce and drag force were calculated after the flow simulation and found out to be 161.253 N and 19.528 N respectively, which can also be seen in Table 6. When the results obtained from 4° angle of attack were compared to those of 0°, it was calculated that the more aggressive set up resulted in a 32.3% increase in downforce and a 52% increase in drag force.

It can be seen clearly that the percentage increase in downforce when attack angle was increased from 0° to 4° is almost double the amount of percentage increase obtained from changing the angle from 0° to 2°. This suggests that the most aggressive angle of attack investigated was more efficient in generating downforce and it could be considered to be in downforce enhancement region with no lift force generation to deteriorate the downforce, eventually leading to catastrophic results. In contrast to downforce enhancement, the drag force was also increased significantly when compared to horizontal set up since there was more surface for the coming air flow to encounter with. This suggests that one must sacrifice better fuel economy, higher top speed, and lower wind noise for higher downforce if the rear wing was to be set up of aggressive attack angles.

If the comparison is to be made between 2° and 4° set ups, it should be mentioned that there was a 13.7% improvement in downforce generation and the drag force acting on the wing was increased by 22.8%. The efficiency of any aerodynamic enhancing device cannot only be decided solely by downforce and drag figures but the ratio between the two is also necessary.

The downforce-to-drag calculations listed in Table 6 strongly suggest that the horizontal set up was the most efficient in overall aerodynamic set up. Even though 0° wing did not generate as much downforce as 4° wing, the D/F_D ratio was calculated to be higher; with 9.4 for 0° and 8.3 for 4°. The higher D/F_D ratio of 9.4 suggests that the higher possible downforce with the minimum generation of drag, and as this aerodynamic efficiency of the rear wing design was achieved at 0° angle attack, the efficiency of the S1223 aerofoil profile at horizontal set ups was once more proven to be true.

When comparing the two higher attack angle settings; 2° and 4°, the aerodynamic efficiency of the rear wing was not extremely affected. With only a difference of 0.6 between the D/F_D ratios of those two settings; 8.9 for 2° attack angle and 8.3 for 4° attack angle, it would be beneficial in real-life applications to use the rear wing at 0° angle of attack during daily driving and at 4° angle of attack at more performance focused driving such as track days. The wing set up can be fixed at the most aggressive angle for better downforce and handling during tracking where fuel efficiency and ride comfort are simply not considered to be defining factors.

The middle setting of 2° angle of attack has got the potential to be beneficial on road applications as well, where the rear wing can be controlled with programming and driving modes to alter its angle according to velocity to provide better stability at higher cruising speeds, without compromising the economy and comfort by a great extent. Additionally, at higher cruising speeds economy and comfort can be disturbed by various other aspects such as vehicle weight, body shape, powertrain option, and suspension setting.

4.5.2 Velocity and Pressure Contours

When the velocity contours through the mid-section of the three different wing set ups were observed, it can be deduced that the 0° wing appeared to be more successful in terms of achieving a smoother air flow around the aerofoil. The velocity contour in Figure 26 shows that the velocity of the air flow was efficiently lowered, nearly as low as 0 m/s, on the pressure and suction surfaces of the wing. Moreover, the velocity was distributed evenly throughout the both surfaces of the wing, with no sudden increases in the velocity at certain locations which may lead to turbulent behaviour.

Figure 26 also suggests that the velocity of the air started to increase towards the trailing edge of the wing as expected, after it reaches the stagnation point on the leading edge. The stagnation point can be clearly seen in Figure 27. The velocity and the pressure contours of the 0° angle wing in Figures 27 and 28 additionally suggested that the wing obeyed the Bernoulli's Principle sufficiently. The velocity of the air flow through the suction surface of the wing was higher with lighter blue sections on the velocity contour, when compared to the air flow through the pressure surface. The pressure contour dictated that the pressure beneath the suction surface was effectively lower with a negative pressure zone, resulting in suction from the higher-pressure zone above the wing to the lower-pressure zone underneath. As a result, negative lift, hence downforce was generated.

When the velocity and pressure contours of the 2° angle wing were studied in Figures 32, 33, 34, similar behaviour to the 0° angle wing was observed. However, the velocity distribution through the pressure and suction surfaces of the wing was seen to be more catastrophic. This was of course due to the higher angle of attack. Figure 32 showed

that the air flow velocity started to increase at a location closer to the leading edge, in comparison to the 0° angle set up.

Slightly after the stagnation point, the velocity distribution started to become deteriorated. Figure 32 showed that the transition to turbulent flow on the wing surfaces was about to happen, where a slight disturbance on the air flow can be seen on the pressure surface of the wing near the leading edge, and the air flow lost its laminar nature on the suction surface towards the trailing edge. On the other hand, fully turbulent flow was not observed on the mid-section of the wing since the flow simulation data showed no eddy currents being formed on the middle section. It can also be seen on Figure 32 that the flow velocity was much higher on the pressure surface towards the trailing edge, when compared to Figure 26 of the 0° angle wing.

Furthermore, the pressure contour of the 2° set up displayed on Figure 34 provided a similar result as of the 0° angle wing. The pressure underneath the suction surface was effectively lower than that on the upper surface. However, higher velocity suggests that the pressure should be higher as well. Additionally, as the velocity was distributed on the 2° angle wing as evenly as the 0° angle wing, it is safe to say that the pressure distribution around the rear wing was not as smooth at 2° angle of attack.

On the other hand, the wing performed sufficiently at 2° angle of attack since there was no eddy currents through mid-section and the wing did not stall. The wing may have also been benefitted from the suitability of the S1223 aerofoil to the low Reynolds number flow.

Looking at Figures 38, 39, and 40, the wing at the most aggressive setting of 4° angle of attack behaved similarly to when the wing was at 2°. However, the velocity profile resembled that of 0° angle wing even though the angle of attack was the most aggressive of the three tested. Fluctuations in the velocity profile was still observed, especially on the pressure surface of the wing closer to the trailing edge, but the flow velocity did not go up right after the stagnation point as it did for the 2° angle wing.

The velocity contour in Figure 38, resembled the flow characteristics of a laminar flow. Hence, it is safe to say that the air flow on the pressure and suction surfaces of the wing was laminar through the leading edge, although it seemed to enter a transition phase towards the trailing edge where the increase in flow velocity was mostly took place.

When comparison was made between Figures 32 and 38, the suction surface of the wing, 4° angle of attack was more successful at keeping the air flow attached through the mid-section of the wing. Whereas in the case of 2° angle of attack, the velocity of the air underneath the wing seemed to fluctuate up an extent.

The pressure contour in Figure 40 showed that the 4° angle wing acted similarly to the previous cases, where there was a negative pressure zone on the suction surface and the local pressure was relatively higher on the upper surface of the wing. Even though the velocity contour of the 4° angle wing showed that it managed to retain a smoother velocity distribution than the 2° angle wing, the D/F_D data showed otherwise where the 2° angle of attack was more aerodynamically efficient. However, as it was mentioned before the difference between the two was calculated to be negligible, especially when the higher downforce generation of the 4° angle wing was considered.

Observing the stagnation points on the horizontal and 4° angle of attack wing in Figures 27 and 39, it was clear that the stagnation point for the 0° angle of attack case appeared to be located closer to the suction surface of the wing. Whereas for the 4° angle of attack case, the stagnation point was found to be near to the very tip of the wing, closer to the pressure surface. This may suggest that more air particles were carried through the pressure surface of the wing at 4°, resulting in higher velocity on the upper surface towards the trailing edge. If the flow velocity was to be increased at aggressive attack angle settings, it was likely that the wake region will take place through the mid-section of the wing.

4.5.3 Velocity Vectors and Streamlines

Once the Figures 29 and 30 were observed, it has been revealed that the air flow did not completely attach to the pressure surface of the wing, on the middle section. The flow appeared to have passed over the trailing edge, whereas it was successfully attached on the leading edge after the stagnation point. However, this was an expected response by the wing since turbulent air flow was simulated to flow around the rear wing, rather than a perfect laminar flow.

The air flow followed the profile of the suction surface of the 0° angle wing more successfully, and the air flow was attached right on the lower surface starting from the leading edge to the trailing edge. This suggests that a laminar boundary layer must have been present on the suction surface of the wing 0° angle of attack and the flow passing over the pressure surface was more chaotic in its nature. On the other hand, Figure 26 together with the D/F_D values in Table 6 suggested the most complete air flow has been achieved at 0° angle of attack.

The velocity vectors of 0° angle wing in Figure 29 revealed similar results to the streamlines in Figure 30. The velocity of the air flow increased right after the flow reached the stagnation point, and the air particles accelerated at angle to the chord line of the wing, leading to flow separation on the pressure surface towards the trailing edge. However, the streamline plots showed no reversed flow, hence eddy current, through the middle section. This once again suggests that the air flow was going through a transition phase however never went completely turbulent after the trailing edge through the mid-plane of the wing. Of course, this could also be explained by the low Reynolds number of the flow and low inlet velocity.

The majority of the turbulence was caused by the side section of the rear wing, the resulting eddies can be observed in Figure 31. Rear wings are known to generate wake regions trailing through their side plates. Figure 31 showed eddies being formed and the air flow following a clockwise direction on the right side and an anticlockwise direction on the left side of the wing, trailing behind the wing.

The majority of the drag force was of course cause by this as the air flow always wants to stick to the surfaces it passes through. At higher velocity applications, the drag force would increase with the increasing downforce, and the turbulence of caused by the side sections would eventually cause the wing to stall at extremely high Reynold number flows.

Figure 36, revealed somewhat opposite results to those of 0° angle of attack. When the wing was set at 2°, the air flow appeared to be attached more successfully onto the pressure surface, when compared with the suction surface. Air flow remained attach on the suction surface right after the stagnation point, however separation happened

quite early and the flow remained separated all the way through the trailing edge. Nevertheless, the boundary layer on both of the surfaces of the wing was never transitioned fully into turbulent as no reversed flow was observed on the mid-plane of the wing.

Figure 35, when compared to Figure 29 of the 0° angle set up, showed the air particles actually accelerated to a lower velocity after the stagnation point through the upper surface. Flow velocity was observed to be stabilised on the pressure surface towards the trailing edge in Figure 35, but the opposite happened beneath the suction surface where the flow appeared to gain velocity as it reached the trailing edge. This potentially explained the fluctuation observed under the wing at the trailing edge, in the velocity contour of the 2° angle wing in Figure 32. The sudden local increase in the flow velocity near the leading edge seen in Figure 32 was also enlightened by the velocity vector plot in Figure 35.

Moving to the flow behind the trailing edge, Figure 37 of the 2° angle of attack set up showed similar results to Figure 31, where the turbulence was mostly caused by the side sections of the rear wing.

Looking at the streamlines over the 4° angle of attack set up in Figure 42, it can confidently be mentioned that the most aggressive angle attack tested was in fact the most successful setting in achieving an attached flow around the aerofoil profile. The air flow was observed to be completely attached to the pressure surface of the wing, suggesting a perfect laminar boundary layer. Considering the aggressive nature of the associated attack angle, this was quite unexpected since flow separation on either one of the surfaces was observed when the wing was at 0° and 2° attack angle.

On the other hand, it would be false to say that flow was attached to the wing on both surfaces since flow separation was observed beneath the suction surface in Figure 42. The nature of the separation appeared similar to the case of 2° angle of attack, where the flow remained attached after the stagnation point up to an extent and the separation happened and remained that way all the way through the trailing edge. This phenomenon once again shined a light onto the slight velocity fluctuations seen in velocity contour of the 4° angle wing in Figure 38.

Vector plot for the 4° angle wing in Figure 41 showed similar behaviour to the velocity vectors of the 2° attack angle case. The velocity of the air particles over the pressure surface was observed to be lower than the air velocity way beneath the suction surface. The air particles were seen to accelerate under the leading edge immediately after the stagnation point, and the opposite behaviour was observed above the leading edge. In fact, the velocity of the air particles was much lower above the leading edge at 4° than the that of 2°. This could be explained by the more turbulent nature of the flow passing under the suction surface.

Overall, the flow appeared to slow down toward the trailing edge and although flow separation was seen on the suction surface, the boundary layer did not transition into a fully turbulent nature since no reversed flow and eddies were observed through the mid-plane, just like the other two set ups. Similar to the 0° and 2° angle set ups, turbulence and hence drag was mainly caused by the side sections of the wing as it can be seen in Figure 43. Nearly the same flow pattern as the previous two settings was observed trailing behind the side sections for the 4° angle of attack.

To sum it all up, same deduction can be made as when the velocity and pressure contours, and the aerodynamic performance calculations were observed. The 0° angle of attack was once again the most aerodynamically efficient setting with flow being attached to either of the surface up to some extent. The 4° attack angle, on the other hand, was highly effective in keeping the flow completely attached on the upper surface of the aerofoil from the leading edge all the way through the trailing edge. The 2° attack setting was however, was once again proven to be insufficient for high performance applications under the light of all the findings, but still has got the potential to be used as a stability device for the road during faster cruising.

4.5.4 Aerodynamic Behaviour of the Wing at Negative Angle of Attack

The wing provided surprising results when it was tested at -4° angle of attack. The velocity contour in Figure 37 showed similar behaviour to the velocity contour of the 4° angle wing in Figure 31. The velocity of the flow was relatively low at the leading edge after the stagnation point on both surfaces of the wing. However, the flow velocity on the pressure surface of the wing appeared to accelerate towards the trailing edge, causing majority of the turbulence behind the wake region which can also be seen in Figure 40 with the vortices.

The pressure contour in Figure 38 on the other hand displayed highly dissimilar results compared to the pressure contours of the other three attack angles tested. The overall pressure around the wing was seen to be generally higher with orange-coloured sections, however there was still a low-pressure zone underneath the suction surface indicated by a light yellow-coloured section, only with greater local pressure. This suggests that there was suction underneath the wing resulting in negative lift even though the wing was set at a negative angle of attack.

The force components showed interesting results. The -4° angle of attack generated a higher amount of downforce than all other attack angles tested, with 191.818 N. Even though it generated a comparably high drag force of 18.773 N at 30 m/s of inlet velocity, it was still lower than the drag force generated at 4° angle of attack at a lower inlet velocity of 20 m/s. Although the drag force was not as low as the drag force achieved at the horizontal set up of the wing, the downforce to drag force ratio of 10.1 for the negative attack angle suggests that it was even more aerodynamically efficient that the horizontal set up which achieved a ratio of 9.5.

Chapter 5

CONCLUSION

In order to sum everything up, numerous literatures on the importance of aerodynamics in road going vehicles published over the recent years have been reviewed in this paper. Further comparison was made between each reviewed literature and comments was made based on the findings of each individual published work. Where certain literature investigated a road vehicle body, some were interested in the performance of certain aerodynamics enhancing devices; such as rear/front wings, underbody trays, and diffusers.

Once the relevant literatures were reviewed, further investigation was made by simulating turbulent air flow around a rear wing design based on the S1223 aerofoil profile. CFD simulations were performed using the ANSYS Fluent software, where the rear wing design was tested at three different angles of attack; being 0°, 2°, and 4°, to find the best possible setting for the rear wing. The attack angle was kept relatively low on purpose since the S1223 aerofoil profile was specifically designed to generate lift at attack angles as low as 0°. Downforce generation was made possible by simply turning the aerofoil profile upside down.

The wing was placed in an enclosure; whom dimensions can be seen in Table 2, to simulate a wind tunnel environment. The k-ε turbulence model was chosen, and the air was set to flow at 20 m/s through the inlet of the enclosure. Numerous boundary

conditions were set which can be read in Chapter 3 for more detail. After the numerical calculation of the air flow was made, post processing steps were applied on the wing for downforce and drag force calculations, together with flow visualisation.

Under the light of all the calculations and flow visualisation data, it was deduced that the rear wing possessed the highest aerodynamic efficiency in terms of overall performance at 0° and -4° angle of attack. The horizontal setting was commented on to be the most suitable setting for road use due its sufficient downforce generation even at low flow velocities. Additionally, its low drag force generation potentially leads to less wind noise and better fuel efficiency, which are major factors when considering daily driven road vehicles.

The 2° angle of attack setting was also proven to be quite beneficial for street driving, especially if it is to be operated by an adaptive rear wing system. Higher downforce generation that the 0° angle of attack meant that it is suitable for high-speed cruising to provide additional stability to the vehicle, hence improving safety. Additionally, as there was not an extreme difference in drag force between the 2° and 4° settings, the slightly higher drag force than the 0° setting can be negligible at high-speed cruising. Realistically, the rear wing will not be the only factor to cause wind noise and reduce fuel efficiency at legal highway cruising speed limits.

The most aggressive angle tested was concluded to be most performance focused setting. Surprisingly, the 4° angle of attack was found out to be the most successful in terms of keeping the flow attached to the aerofoil. Considering the high downforce generations, and the as downforce increases with increasing velocity, top speed can be compromised for better aerodynamic grip on the track, when one brings their high-

performance vehicle to track days. However, for tracks with relatively longer straights and faster corners where top speed becomes more invaluable, 2° angle of attack still potentially be beneficial without sacrificing speed.

In order to further improve on this study, main turbulence generating parts of the wing, which are the side sections, could be eliminated to obtain a simpler and cleaner design, Additionally, the chord length could be decreased and the span of the wing could be widened to achieve higher aerodynamic efficiency by higher aspect ratio. One other design solution could be designing a multi-element rear wing with a primary and a secondary element. Where both elements would have the same span, the secondary element could have a shorter chord length than the primary elements, and could be positioned at a higher angle of attack. Drag could be reduced at high flow velocities by operating a drag reduction system where the secondary element could be basically set at 0°, allowing the air to pass through.

REFERENCES

[1] H. Flegl and U. Bez, “Aerodynamics - conflict or compliance in vehicle layout?,” no. (Technol. Adv. in Vehicle Des.-Special Publication SP3-1983), 1983.

[2] H. H. Braess H. Burst L. Hamm, and R. Hannes, “Improvement of handlıng characteristics of automobiles by reducing the aerodynamic lift.,” *Automob. Z.*, vol. 77, no. 4 (1975), 1975.

[3] P. Wright and T. Matthews, *Formula 1 Technology*. 2001.

[4] P. G. Wright, “Influence of aerodynamics on the design of formula one racing cars.,” *Int. J. Veh. Des.*, vol. 3, no. 4, 1982, doi: 10.1504/IJVD.1982.061285.

[5] X. Zhang, W. Toet, and J. Zerihan, “Ground effect aerodynamics of race cars,” *Applied Mechanics Reviews*, vol. 59, no. 1–6. 2006, doi: 10.1115/1.2110263.

[6] W. Assmann and L. Witte, “Influence of aerodynamics on the road performance of a passenger car.,” 1982.

[7] K. Kurec, M. Remer, T. Mayer, S. Tudruj, and J. Piechna, “Flow control for a car-mounted rear wing,” *Int. J. Mech. Sci.*, vol. 152, 2019, doi: 10.1016/j.ijmecsci.2018.12.034.

[8] M. S. Genç, I. Karasu, and H. Hakan Açikel, “An experimental study on

aerodynamics of NACA2415 aerofoil at low Re numbers," *Exp. Therm. Fluid Sci.*, vol. 39, 2012, doi: 10.1016/j.expthermflusci.2012.01.029.

[9] C. Fu, M. Uddin, and A. C. Robinson, "Turbulence modeling effects on the CFD predictions of flow over a NASCAR Gen 6 racecar," *J. Wind Eng. Ind. Aerodyn.*, vol. 176, 2018, doi: 10.1016/j.jweia.2018.03.016.

[10] R. Ricci and S. Montelpare, "A quantitative IR thermographic method to study the laminar separation bubble phenomenon," *Int. J. Therm. Sci.*, vol. 44, no. 8, 2005, doi: 10.1016/j.ijthermalsci.2005.02.013.

[11] R. Ricci, S. Montelpare, and E. Silvi, "Study of acoustic disturbances effect on laminar separation bubble by IR thermography," *Exp. Therm. Fluid Sci.*, vol. 31, no. 4, 2007, doi: 10.1016/j.expthermflusci.2005.08.007.

[12] W. Zhang, R. Hain, and C. J. Kähler, "Scanning PIV investigation of the laminar separation bubble on a SD7003 airfoil," *Exp. Fluids*, vol. 45, no. 4, 2008, doi: 10.1007/s00348-008-0563-8.

[13] M. Gaster, "The Structure and Behaviour of Laminar Separation Bubbles," *Aeronaut. Res. Counc. Reports Memo.*, no. 3595, 1967.

[14] I. Tani, "Low-speed flows involving bubble separations," *Prog. Aerosp. Sci.*, vol. 5, no. C, 1964, doi: 10.1016/0376-0421(64)90004-1.

[15] K. Rinoie and N. Takemura, "Oscillating behaviour of laminar separation

bubble formed on an aerofoil near stall," *Aeronaut. J.*, vol. 108, no. 1081, 2004, doi: 10.1017/s0001924000151607.

[16] D. M. Sharma and K. Poddar, "Experimental investigations of laminar separation bubble for a flow past an airfoil," in *Proceedings of the ASME Turbo Expo*, 2010, vol. 6, no. PARTS A AND B, doi: 10.1115/GT2010-22224.

[17] A. Moen, L. Mauri, and V. D. Narasimhamurthy, "Comparison of k-ε models in gaseous release and dispersion simulations using the CFD code FLACS," *Process Saf. Environ. Prot.*, vol. 130, 2019, doi: 10.1016/j.psep.2019.08.016.

[18] T. Morgenstern, T. Petzoldt, J. F. Krems, F. Naujoks, and A. Keinath, "Using European naturalistic driving data to assess secondary task engagement when stopped at a red light," *J. Safety Res.*, vol. 73, 2020, doi: 10.1016/j.jsr.2020.03.007.

[19] T. Morgenstern, L. Schott, and J. F. Krems, "Do drivers reduce their speed when texting on highways? A replication study using European naturalistic driving data," *Saf. Sci.*, vol. 128, 2020, doi: 10.1016/j.ssci.2020.104740.